CROATIAN – USA WORKSHOP
on
MESOMETEOROLOGY

Ekopark Kraš Resort near Zagreb, Croatia

18-20 June 2012

ORGANIZING INSTITUTIONS

Meteorological and Hydrological Service of Croatia
School of Meteorology, University of Oklahoma
Geophysical Institute, University of Zagreb

ABSTRACTS OF PRESENTATIONS BY PARTICIPANTS

ORAL

PRESENTATIONS

Numerical simulation of stable atmospheric boundary layer at high resolution : katabatic flows modeling and processes analysis

Sébastien Blein

Laboratoire des Écoulements Géophysiques et Industriels (LEGI), Grenoble, France

1. Introduction

Turbulence on the very close vicinity of the ground within stable atmospheric boundary layer is often parametrized on numerical atmospheric models commonly used. It could be relatively strong into katabatic flows. The aim of the present work is to better understand the behavior of those flows.

2. Numerical simulation

We study a realistic down-slope flow : we model an existing mountain slope (complex topography) overlooking Grenoble (French Alps). The French model, MesoNH (Meteo-France and Laboratoire d'Aerologie, Toulouse, France, Lafore et al., 1998 [2]) is used in its LES formulation (1.5 order closure scheme : TKE model based on Bougeault and Lacarrere mixing length scale). Simulations are performed at high resolution. The spatial discretisation is of $2m$ at the surface. Horizontaly, the grid size is of $12m$. Time step is set to $0.1s$. The atmospheric initial conditions and external forcing are set from Largeron, 2010 [3]. He highlighted the strong correlation between persistent stable atmospheric conditions (or temperature inversions) and strongly polluted events in this region. The calculation is initialized at $12h$ L.T. on Dec. $26th$, 2006 and run up to $06h$ on Dec. $27th$, 2006.This corresponds to the core of a strongly stable event. The transition regime from the day to the night is caught. We observed the establishment of a well defined katabatic flow. The latter is shown in Fig. 1 as streamlines at a constant distance from the ground ($2m$). The flow on the vicinity of the ground is clearly channeled by the topography. Vertically, the katabatic flow is shown in a vertical section (Fig. 2). Velocity vectors reveal a downslope low-level jet over which a weak reverse current appears.

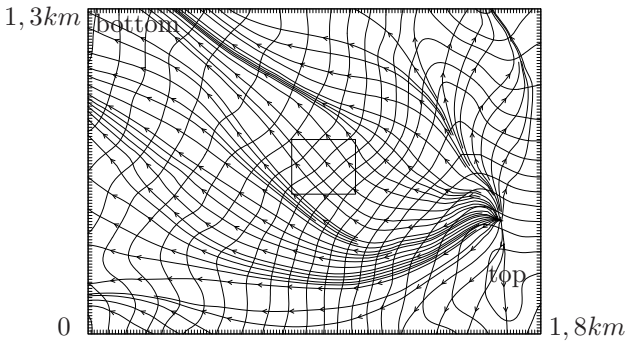

FIGURE 1 – Streamlines (arrows) of the katabatic flow at $2m$ above the ground, topography as contours (lines) and statistical area (central frame).

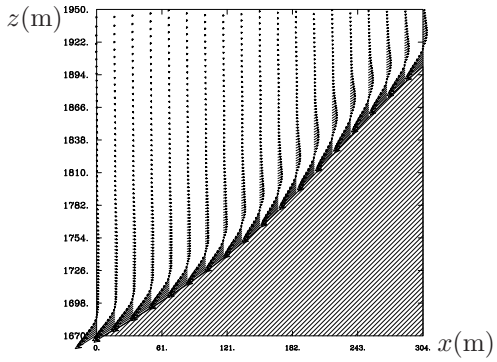

FIGURE 2 – Velocity vectors on a vertical plane along a streamline on the middle of the slope.

3. Prandtl model

Statistics are performed on the present results. Fedorovich and Shapiro, 2009 [1] revisits the well-known Prandtl model (Prandtl, 1942 [4]) in particular in term of boundary conditions (see further). The initial model consists of a one-dimensional, stationary, laminar and viscous slope flow within a stably-stratified fluid. The basic equations, obtained from the Prandtl model equation rewritten in term of temperature deficit θ' are reduced to :

$$-\theta'^* + \frac{\partial^2 u^*}{\partial z^{*2}} = 0 \qquad (1) \qquad\qquad u^* + \frac{\partial^2 \theta'^*}{\partial z^{*2}} = 0 \qquad (2)$$

with the dimensionless variables $z^* = z_n/L$, $u^* = u_n/V$ and $\theta'^* = \theta'/\Theta$. Length, velocity and temperature scales L, V and Θ are to be defined. They are deduced from a three equations system :

$$\frac{\nu V \theta_0}{g \Theta sin\alpha L^2} = 1 \quad (3) \qquad \frac{\nu \Theta}{L^2 \gamma V sin\alpha} = 1 \quad (4)$$

the third one being the bottom boundary condition (eq. 5). α is the slope angle (40°), z_n the normal to the surface direction, u_n the katabatic velocity (tangent to the surface) and θ' the potential temperature deficit ($\theta'(z_n) = \gamma z - [\theta(z_n) - \theta_0]$, with γ the external temperature gradient, z the absolute vertical direction and θ_0 the reference temperature at the surface). θ' represents the difference with the external stratification. Boundary conditions are : $u^*(0) = 0$, $u^* \to 0$ and $\theta'^* \to 0$ for $z_n^* \to \infty$. For the temperature at the ground, a constant temperature deficit flux is chosen here to describe the cooling of the flow :

$$\frac{d\theta'^*(0)}{dz^*} = -\frac{F_s L}{\nu \Theta} = -1 \quad (5)$$

with $F_s = -\nu d\theta'/dz_n$ the ground heat flux. Characteristic scales are defined as : $L^{-1} = (g\gamma)^{1/4} sin^{1/2}\alpha \nu^{-1/2} \theta_0^{-1/4}$, $V^{-1} = g^{-1/4} F_s^{-1} \theta_0^{1/4} (\nu sin\alpha)^{1/2} \gamma^{3/4}$ and $\Theta^{-1} = F_s^{-1} \theta_0^{-1/4} (g\gamma)^{1/4} (\nu sin\alpha)^{1/2}$. With consistent control parameters, values are : $L \approx 4m$, $V \approx 7m.s^{-1}$ and $\Theta \approx 2K$. This equation system has the solution plotted in thick solid lines Fig. 3 (potential temperature deficit) and Fig. 4 (katabatic velocity). When radiative cooling at the surface is sufficient, a katabatic flow is observed as a few meters thick wall-jet with a maximum speed of few meters per second. It is observed in both Prandtl model which described an idealized configuration and numerical simulation of a realistic thus complex configuration (complex and steep orography, inhomogeneous radiative forcing, not at rest initial condition although weak synoptic forcing...). To assess the validity of the Prandtl approach in such a configuration, the simulation results are averaged in time ($360s$) and space (horizontaly on a $252 \times 216 m^2$ area). At each vertical level, it means the use of $n_x \times n_y \times n_t \approx 1.4e6$ samples. The averaging area is represented by the frame Fig. 1, where streamline are normal to the contours. It make this area closer to the Prandtl configuration (one dimensional flow approximation). Mean profils of $\theta'^*(z^*)$ and $u^*(z^*)$ are shown as thin lines Fig. 3 and 4. The computed flow show interesting similarities with the Prandtl model.

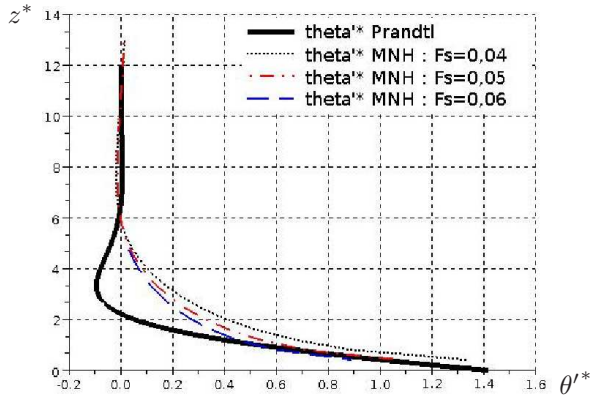

FIGURE 3 – Mean profiles of normalized temperature deficit from simulations (thin lines) and from the Prandtl model (thick line).

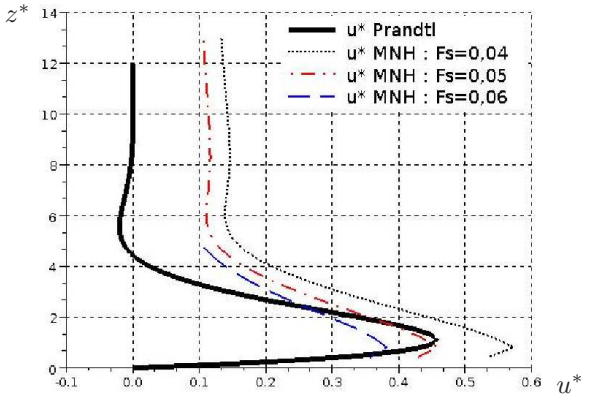

FIGURE 4 – Mean profiles of normalized velocity from simulations (thin lines) and from the Prandtl model (thick line).

Results have also revealed interesting turbulent structures on the external gradient of the low-level jet. The forthcoming work is based on characterizing the various processes on natural thus complex configuration.

Références

[1] E. Fedorovich and A. Shapiro. Structure of numerically simulated katabatic and anabatic flows along steep slopes. *Acta Geophysica*, (57) :981–1010, 2009.

[2] J.P. Lafore, J. Stein, N. Asencio, P. Bougeault, V. Ducrocq, J. Duron, C. Fischer, P. Hereil, P. Mascart, V. Masson, J.P. Pinty, J.L. Redelsperger, E. Richard, and J. Vila-Guerau de Arellano. The meso-nh atmospheric simulation system. part i : adiabatic formulation and control simulation. In *Annales Geophysicae*, 1998.

[3] Y. Largeron. Dynamique de la cla stable en relief complexe. application aux episodes de pollution particulaire des vallees alpines. In *PhD Thesis*, 2010. Université Joseph Fourier, Grenoble.

[4] L. Prandtl. Furer durch die stromungslehre. In *Vieweg und Sohn, Braunschwieg*, 1942.

Comparison of convective boundary layer velocity spectra calculated from large eddy simulation and WRF model data

Jeremy A. Gibbs* and Evgeni Fedorovich*

*School of Meteorology, University of Oklahoma, Norman, Oklahoma, USA

1. Introduction

The Weather Research and Forecasting (WRF) model (Skamarock et al. 2008) has evolved toward a self-contained numerical weather prediction system, capable of modeling atmospheric motions ranging from global to microscales. The promise of such capability is appealing to both operational and research environments where accurate prediction of turbulence is increasingly desirable. However, the ability of the WRF model to adequately reproduce small-scale atmospheric motions in the range of scales of the order of 100 m and smaller remains questionable.

2. Approach

In this study, turbulent flows in the dry atmospheric convective boundary layer (CBL) were reproduced using a traditional large eddy simulation (LES) code (OU-LES; Fedorovich et al. 2004a,b) and the WRF model applied in an LES mode (WRF-LES). Simulations were run in a numerical domain of $10.24\times10.24\times2$ km^3 and were initialized with the same idealized vertical profiles of velocity, temperature, and moisture. The respective CBL forcings were set equal and held constant. Both codes use 3rd-order Runge-Kutta time integration scheme and 1.5-order subgrid turbulence kinetic energy closure scheme. The effects of CBL flow types (with and without shear) and of varying isotropic grid spacing (from 20 m to 80 m) were investigated.

3. Description of experiments

Horizontal slices of velocity fields were obtained from simulation data to enable comparison of CBL flow patterns. Two-dimensional spectra calculated from the turbulent velocity fluctuations were used to characterize the planar turbulence structure, following Kelly and Wyngaard (2006). One-dimensional velocity spectra were also calculated following Kaiser and Fedorovich (1998).

4. Results

One- and two-dimensional *u*-component velocity spectra from conducted simulations are presented in Fig. 1. Results show that the WRF model tends to attribute slightly more energy to larger-scale flow structures as compared to the CBL reproduced by OU-LES. This is confirmed through visual inspection of horizontal velocity slices (not shown), in which WRF-LES produces larger-scale, streakier turbulent structures.

Consequently, the WRF model fails to adequately reproduce spatial variability of velocity fields within broader scale ranges. For instance, in the shear-driven CBL simulation with grid spacing of 20 m, OU-LES produced a velocity variance of 0.51 m^2s^{-2}, while WRF-LES only produced a variance of 0.33 m^2s^{-2}. Spectra from WRF-LES typically have narrower inertial spectral subranges and point to enhanced dissipation of turbulence on small scales of motion. This divergence of high-frequency spectral signals between OU-LES and WRF-LES data occurs consistently at wavelengths corresponding to approximately 7 to 10 times the grid spacing, a feature noted in a study by Skamarock (2004).

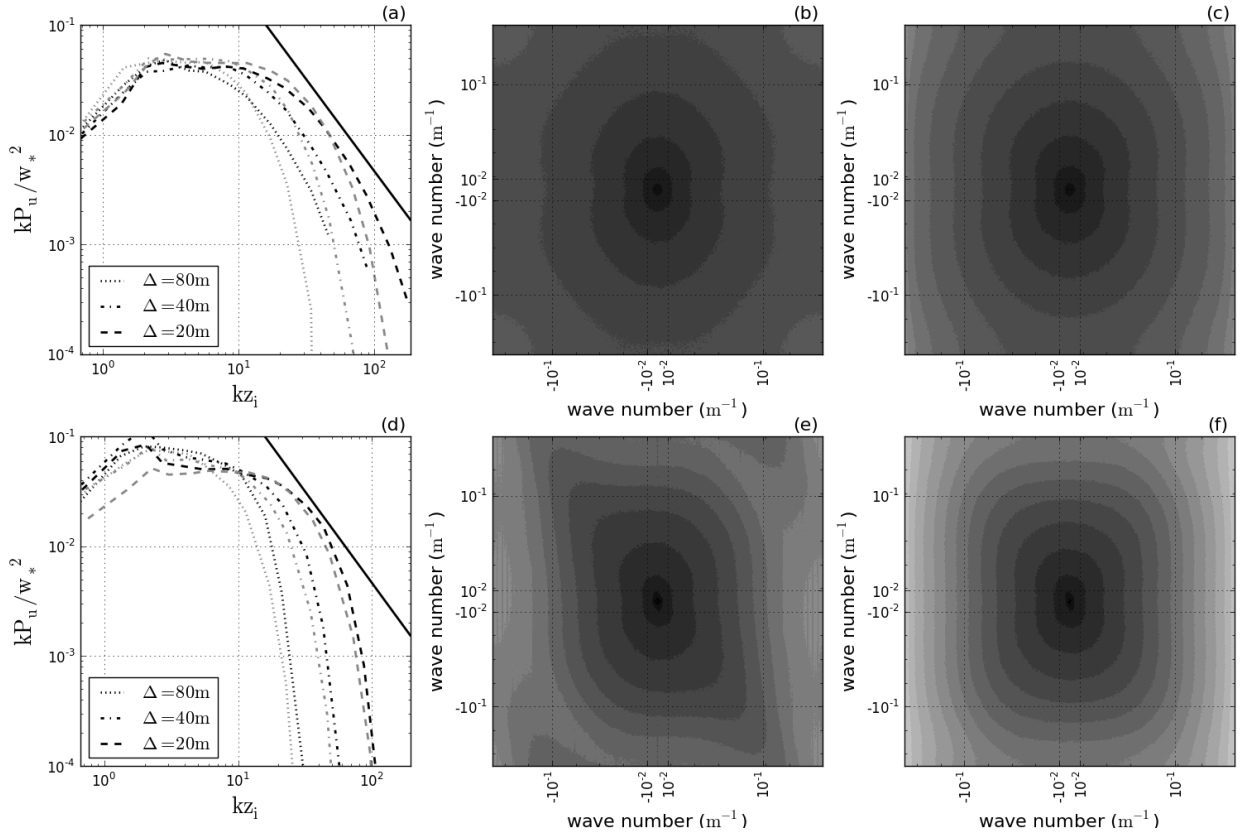

Figure 1: Normalized one-dimensional *u*-component velocity spectra from OU-LES and WRF-LES of shear-free (a) and sheared (b) CBL flows with 20-m, 40-m, and 80-m grid spacing. Straight solid lines in (a) and (d) correspond to the -5/3 law. The corresponding two-dimensional *u*-component velocity spectra from OU-LES (b, e) and WRF-LES (c, f) with grid spacing of 20 m are also shown. Darker colors represent larger spectral density values. Shown spectra refer to the quarter-CBL-depth level.

5. Discussion

Results from LES of different CBL flow types with varying grid spacing consistently demonstrate that the WRF-LES velocity fields are overly dissipative on smaller scales of motion. The WRF model is based on fully compressible equations of motion, while OU-LES employs the incompressibility assumption and solves equations of flow dynamics in the Boussinesq approximation. It is possible that implicit filtering applied in the time-splitting procedure for removal of acoustic modes in the WRF model causes the considered over-damping effect that may represent an inherent limitation of WRF-LES.

References

Fedorovich, E., R. Conzemius, and D. Mironov, 2004a: Convective entrainment into a shear-free, linearly stratified atmosphere: Bulk models reevaluated through large eddy simulations. *J. Atmos. Sci*., **61**, 281-295.

——, and Coauthors, 2004b: Entrainment into sheared convective boundary layers as predicted by different large eddy simulation codes. *Preprints, 16th Symp. on Boundary Layers and Turbulence*, Portland, ME, Amer. Meteor. Soc., P4.7.

Kaiser, R., and E. Fedorovich, 1998: Turbulence spectra and dissipation rates in a wind tunnel model of the atmospheric convective boundary layer. *J. Atmos. Sci.*, **55**, 580-594.

Kelly, M., and J. C. Wyngaard, 2006: Two-dimensional spectra in the atmospheric boundary layer. *J. Atmos. Sci*., **63**, 3066-3070.

Skamarock, W. C., 2004: Evaluating mesoscale NWP models using kinetic energy spectra. *Monthly Weather Review*, **132**, 3019-3032.

Tornadogenesis in a Simulated Mesovortex: The Role of Surface Friction

Alexander D. Schenkman, Ming Xue, and Alan Shapiro

School of Meteorology, University of Oklahoma, Oklahoma, USA
Center for Analysis and Prediction of Storms, University of Oklahoma, Norman, OK

1. Introduction

A recent paper by Schenkman et al. (JAS, conditionally accepted) has revealed a critical role of surface drag in the development of a tornado-like vortex (TLV) in a high-resolution simulation mesovortex initialized by assimilating real data. More specifically, the concentration of low-level inflow horizontal vorticity behind a gust front leads to the creation of an intense rotor just behind and parallel to the gust front. Backward trajectory analysis reveals that this low-level inflow horizontal vorticity was generated by surface drag. Strong convergence between the westerly flow on the bottom of the rotor and the easterly flow associated with an occluding rear-flank gust front lead to the development of an intense low-level updraft in the upward branch of the rotor. TLV genesis occurs owing to intense stretching of the vertical vorticity associated with the simulated mesovortex. Figure 1 presents a conceptual model summarizing the TLV genesis of this case.

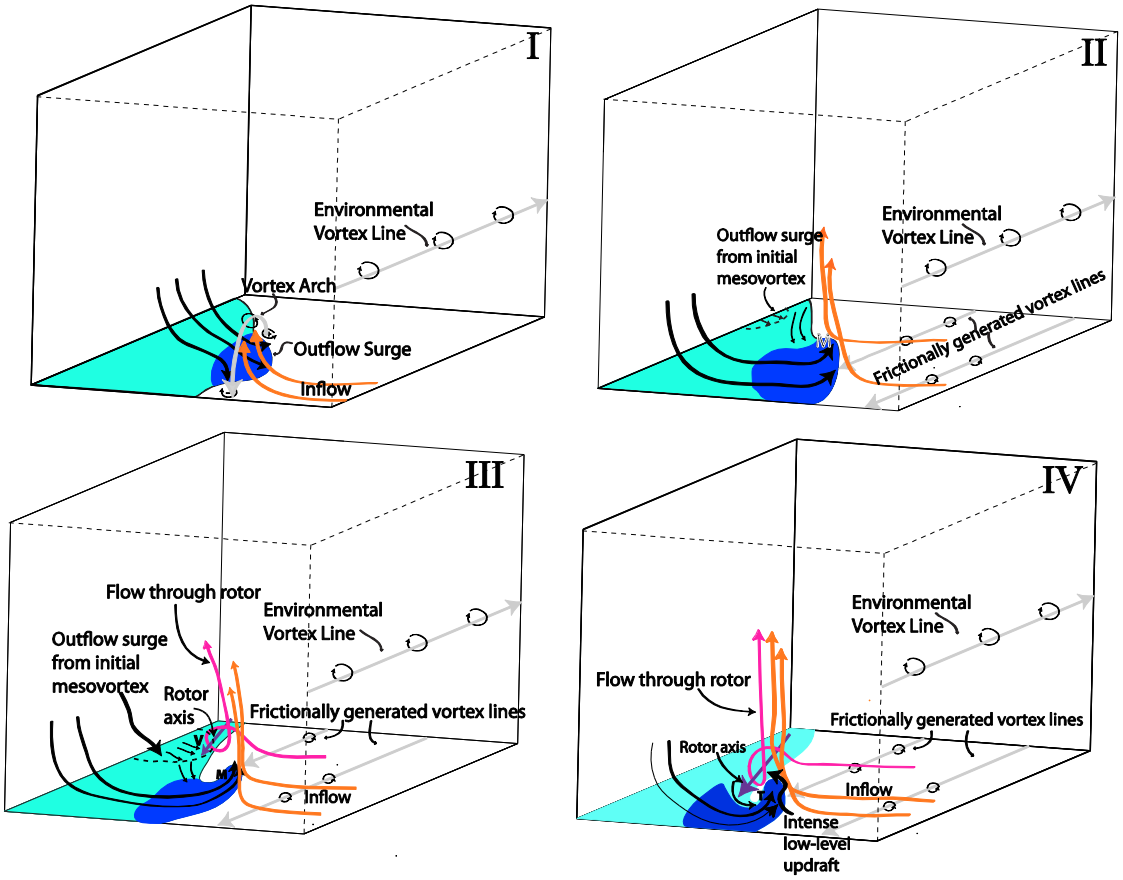

Figure 1. Four-stage conceptual model of TLV genesis in the simulated mesovortex. (I) depicts the development of a gust front bulge which leads to the formation of a vortex arch. In (II), the development of the dominant cyclonic mesovortex and frictionally-generated vortex lines is shown. The development of the rotor owing, in part, to an outflow surge from a previous mesovortex is shown in (III). Finally, TLV genesis is shown as the mesovortex becomes collocated with the upward branch of the rotor in (IV).

2. Generality of results

The substantial role played by surface drag in the above discussed simulation begs the question: How often do such a rotor circulations develop in tornadic storms? While fully answering this question would require detailed sensitivity studies of numerous other cases, we offer some speculative observations in order to possibly provoke others to look for similar features. First off, we note that the environmental conditions associated with the simulated mesovortex are likely not too dissimilar from many other nocturnal mesoscale convective systems associated with tornadoes. Namely, the atmosphere was quite moist over a great depth and featured moderate wind shear (not shown). There was not a large amount of surface-based instability as, near the MCS, the low-levels were stably stratified due to earlier rain and the nocturnal nature of the event. Given these conditions it seems fairly likely that a strong layer of frictional vorticity should develop in the enhanced inflow into a mesovortex/associated convective cell. Whether or not this vorticity is frequently concentrated into a rotor circulation is unknown. Unfortunately, there is little observational evidence to indicate the presence, or lack thereof, of rotors in tornadic mesovortex cases. There is some observational evidence of an enhanced layer of near surface shear associated with surface drag. For example, Dowell and Bluestein (1997) found very strong shear in wind observations from a 440-m tall instrumented tower in the near-updraft supercell inflow (see their Fig. 18). Numerical simulations investigating the impact of anvil shading in supercells (Frame and Markowski 2010) found a similar flow profile which was attributed to surface drag slowing the near-ground flow.

In attempt to determine whether a similar rotor feature could be present in supercells, we have recently begun preliminary examination of a high-resolution simulation of the 8 May 2003 Oklahoma City tornado. This simulation is nested within the simulations of Hu and Xue (2007) and produces two tornado-strength vortices. However, while we note a strong area of enhanced horizontal vorticity in the near-updraft inflow, it does not appear that this vorticity is being concentrated or playing a substantial role in the tornadogenesis in this simulation. At this point in our analysis no rotor circulation is evident.

Additional simulations of non-supercell mesovortex tornadoes would help determine whether a rotor circulation is common in these events. In-depth observational studies may also, at least indirectly, find evidence of such circulations. Such numerical and/or observational studies may be the subject of future work.

References

Dowell, D.C. and H.B. Bluestein, 1997: The Arcadia Oklahoma storm of 17 May 1981: Analysis of a supercell during tornadogenesis. *Mon. Wea. Rev.*, **125**, 2562-2582

Frame, J. and P.M. Markowski, 2010: Numerical simulations of radiative cooling beneath the anvils of supercell thunderstorms. *Mon. Wea. Rev.*, **138**, 3024-3047.

Hu, M. and M. Xue, 2007: Impact of configurations of rapid intermittent assimilation of WSR_88D radar data for the 8 May 2003 Oklahoma City tornadic thunderstorm case. *Mon. Wea. Rev*, **135**, 507-525.

Schenkman, A. D., M. Xue, and A. Shapiro, 2012: Tornadogenesis in a simulated mesovortex within a mesoscale convective system. *J. Atmos. Sci.*, conditionally accepted.

Simulating supercell thunderstorms in a convective boundary layer

Christopher J. Nowotarski* and Paul M. Markowski*

**Pennsylvania State University, University Park, Pennsylvania, USA*

1. Introduction

Most previous numerical simulation studies of supercell thunderstorms have used a horizontally homogeneous environment and exclude radiation and surface fluxes of heat, moisture, and momentum. However, the environment of most supercell thunderstorms is characterized by a turbulent convective boundary layer (CBL) driven by these fluxes. Because of the large vertical wind shear typically found at low levels in supercell environments, the CBL is often organized into horizontal convective rolls (HCRs, see Etling and Brown 1993). HCRs are associated with horizontal variations in parameters such as low-level moisture, potential temperature, and wind shear that are known to be important to supercell evolution (Markowski and Richardson 2007). As such, we expect that supercells simulated in a CBL with HCRs will behave differently than those in a horizontally homogeneous environment typically used in supercell simulations.

2. Method

Simulations are performed using the moist nonhydrostatic cloud model, CM1 (Bryan and Fritsch 2002). Three types of simulations are performed and labeled "CBL Fixed", "CBL Evolve" and "Control" in a methodology similar to Nowotarski et al. (2011). In the CBL simulations, supercells are initiated with a 3 K warm bubble perturbation in a environment with HCRs oriented perpendicular to storm motion. In CBL Fixed, radiation tendencies are fixed to the initial values at storm initiation, while in CBL Evolve they are updated every 300 s. Thus, cloud shading effects are eliminated in CBL Fixed while allowed in CBL Evolve. The Control simulation has full surface physics and radiation is fixed as in CBL Fixed, but storms are initiated in a horizontally homogeneous environment devoid of HCRs. Each simulation is run for 7200 s.

3. Results

Bulk measures of storm strength, such as maximum vertical velocity and vertical vorticity are relatively similar over time at both low-levels and aloft in all three storms (Figure 1). The notable exception is that maximum vertical vorticity is weaker in the Control than in the CBL simulations after 60 minutes (Fig. 1b); however, this result is not found in simulations with parallel rolls (not shown).

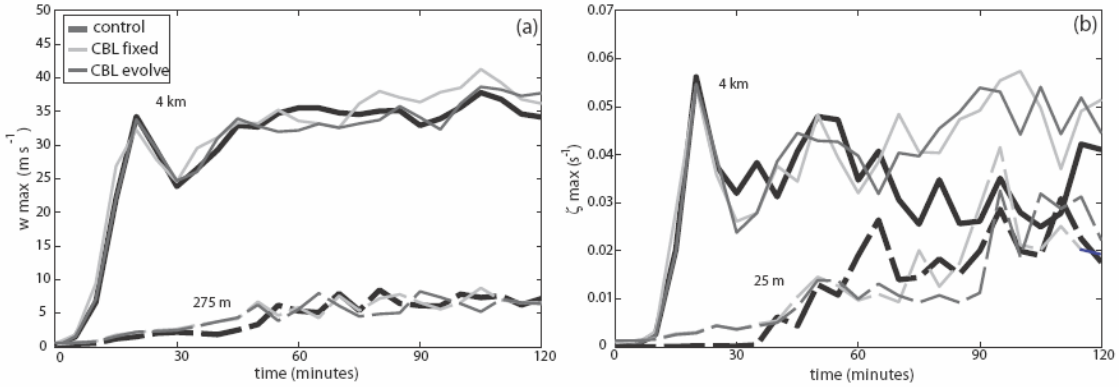

Figure 1. Time series of (a) maximum vertical velocity and (b) maximum vertical vorticity at low (dashed) and mid (solid) levels in the right-moving supercell of each simulation.

Low-level horizontal cross sections of each storm near its time of maximum near-surface vertical vorticitiy (Fig. 2) show that all three storms develop a low-level mesocyclone. However, CBL Fixed develops evenly spaced misocyclone-like circulations along its rear flank gust front (RFGF) that correspond to HCR intersections. Areas of pre-existing vertical vorticity are associated with the HCRs, and at times appear to be ingested into the low-level mesocyclone (Fig. 2b). The control simulation tends to have a more sheet-like arrangement of vorticity along the RFGF (Fig. 2a). The CBL Evolve simulation has weaker HCRs near the storm, likely owing to cloud shading. As such, it has a morphology that is somewhat intermediate to the Control and CBL Fixed storms.

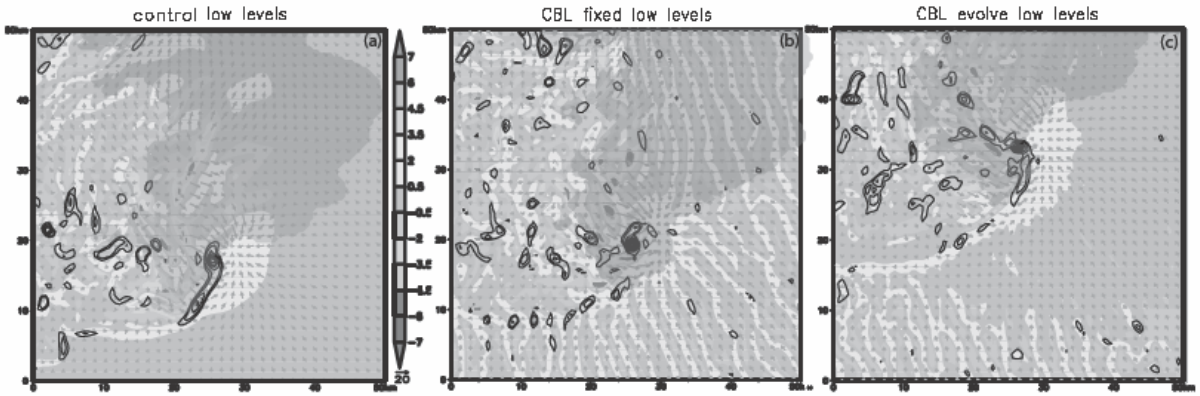

Figure 2. Horizontal cross sections of 275 m above ground level (AGL) vertical velocity (shaded), 25 m AGL vertical vorticity (contours), 25 m horizontal wind (vectors), and 1 km AGL simulated reflectivity greater than 1 dbz (shadow).

At midlevels (not shown), the storms display a spatial correlation between vertical velocity and vertical vorticity typical of a mesocyclone. However, the Control has a more steady (in time) organization of midlevel structure whereas the CBL simulations are both more unsteady, though at most times they have stronger midlevel rotation.

Finally, the storms themselves influence the boundary layer. Shading under the anvil cloud cools the surface in the CBL Evolve case such that boundary layer convection there is diminished (Fig. 2c). Where rolls exist close to the storm in the CBL fixed simulation, strong convergence in the storm inflow advects momentum associated with the rolls towards the storm, causing them to "bend" towards the low-level updraft (Fig. 2b).

5. Conclusions

Whereas bulk measures of storm strength are relatively unchanged, the presence of HCRs in a supercell environment appears to have an effect on small scale vorticity structures at low levels, especially along storm gust fronts. HCRs may also provide a source of pre-existing vorticity to the low-level mesocyclone. Thus, the development of low-level rotation in supercells may be influenced by boundary layer features. However, when the inflow region is shaded by cloud, boundary layer convection is suppressed and may be less influential on storm evolution.

References

Bryan, G. H., and J. M. Fritsch, 2002: A benchmark simulation for moist nonhydrostatic numerical models. *Mon. Wea. Rev.*, **130**, 2917-2928.

Etling, D., and R. A.Brown, 1993: Roll vortices in the planetary boundary layer: A review. *Bound. Layer Meteor.*, **65**, 215-248.

Markowski, P. M. and Y. P. Richardson, 2007: Observations of vertical wind shear heterogeneity in convective boundary layers. *Mon. Wea. Rev.*, **135**, 843-861.

Nowotarski, C. J., P. M. Markowski, Y. P. Richardson, and G. H. Bryan, 2011: Interactions between simulated supercell thunderstorms and dry boundary layer convection. Preprints, *14th Conf. on Mesoscale Processes*, Los Angeles, CA, Amer. Meteor. Soc.

Wave-induced boundary-layer separation: A case study comparing airborne observations with results from a mesoscale model

Lukas Strauss[1], Stefano Serafin[1], Vanda Grubišić[1,2]

[1]*Department of Meteorology and Geophysics, University of Vienna, Vienna, Austria*
[2]*Earth Observing Laboratory, National Center for Atmospheric Research, Boulder, CO*

1. Introduction

Wave-induced boundary-layer separation (BLS) results from the adverse-pressure gradient forces exerted on the atmospheric boundary layer by internal gravity waves in flow over orography. BLS has received significant attention in recent years, particularly so, because it is a key ingredient in the formation of atmospheric rotors (Doyle and Durran, 2002). Traditionally depicted as horizontal eddies in the lee of mountain ranges, rotors develop from the interaction between internal gravity waves and the atmospheric boundary layer. Our study is based on the first observationally documented case of wave-induced BLS, which occurred on 26 January 2006 in the lee of the Medicine Bow Mountains in SE Wyoming (USA). Observations from the University of Wyoming King Air (UWKA) aircraft, in particular, the remote sensing measurements with the Wyoming Cloud Radar (WCR), reveal strong wave activity, downslope winds in excess of 30 ms^{-1}, and rotor formation in the lee of the mountain range (Haimov et al., 2008).

2. Mesoscale modelling of the event

In order to gain insight into the dynamics of the observed event and understand the mesoscale triggers of wave-induced BLS, we employ the Weather Research and Forecast (WRF) model. The model is set up with horizontal grid increments of 400 m and vertical grid increments stretching from 20 m to 340 m. The simulation is initialised with ECMWF analysis data at 12 UTC on 26 Jan, around 6 hours before the time of the observations. Results from the model underpin the expected concurrence of the essential processes leading to BLS (Fig. 1): the breaking of a large hydrostatic wave between 2000 and 5000 m above mountain top provides the conditions for a downslope windstorm to develop along the lee slope of Medicine Bow Range. Further downstream, a hydraulic jump forms with its adverse pressure gradients forcing the detachment of the boundary layer and ensuing rotor formation.

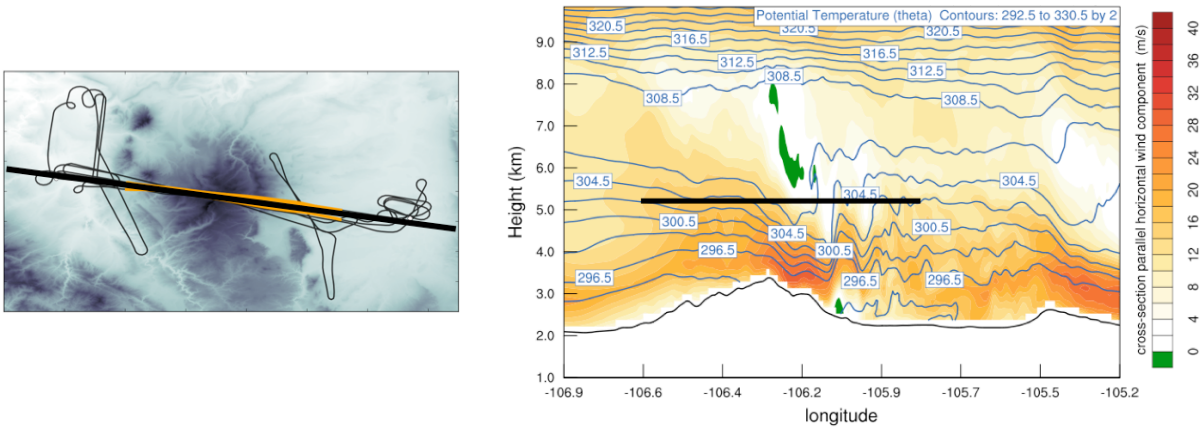

Figure 1. Left panel: topography of Medicine Bow Mountains, SE Wyoming (USA). The continuous thin black line indicates the research aircraft flight track flown on 26 January 2006. Orange lines represent straight passes flown over the mountain peak. Model results are extracted along the thick black line. Right panel: along-track vertical cross-section through the model domain at 21:45 UTC. Blue isentropes and colour shades of along-track horizontal wind. Green patches indicate regions of reversed flow. The thick black line represents a flight pass.

3. Model verification

To the end of verifying the mesoscale model we compare wind and potential temperature extracted from the model along the flight tracks with the observations. The agreement in upstream conditions from the aircraft ramp sounding and the model is satisfactory. The model reproduces the important characteristics of the upstream profile: a lower-level wind jet, almost unidirectional wind and constant stability at the lower and mid-levels. Comparison of in situ measurements and model results along a straight flight pass shows remarkable matching in horizontal and vertical wind and potential temperature for the upstream part of the pass and (expected) poorer matching for the downstream part which was flown through the wave breaking region.

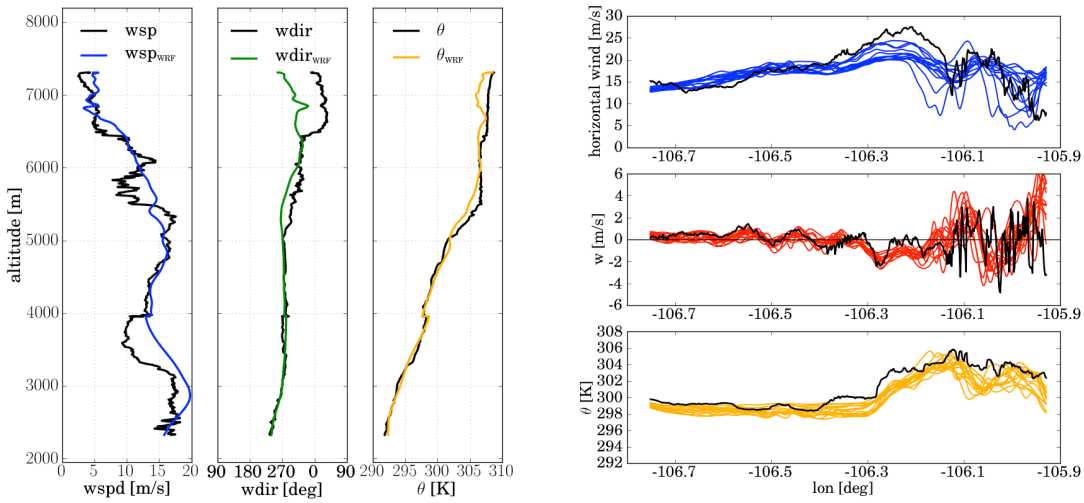

Figure 2. Black lines: aircraft in situ measurements; coloured lines: model data. Left panel: upstream (ramp) sounding. Right panel: data along one flight pass. Model data within a time window of ±1.5 h around the observation time underlines the small (large) model spread of wind speed, w, and θ for the upstream (downstream) part of the leg.

4. Summary and outlook

Some light is shed on the important dynamical processes at work during a real case of wave-induced BLS with the help of mesoscale modelling of the event. A detailed comparison between observations and model results shows fairly good agreement and provides confidence in the ability of the model to reproduce the complex interaction of mountain waves and the boundary layer accurately.
More interesting flow dynamics that were not captured by the observations get apparent from the model in a region north of the aircraft flight legs. Pulsations in the downslope winds, with the same characteristic period of 10-15 min recently reported in a numerical study of Bora wind (Belušić et al., 2007), together with pulsations in the near-surface reversed flow within the rotor are at the focus of future research on the topic.

References

Belušić, D., M. Žagar and B. Grisogono, 2007: Numerical simulation pulsation in the bora wind. Q. *J. R. Meteorol. Soc.*, **133**, 1371-1388.

Doyle, J.D., D.R. Durran, 2002: The dynamics of mountain-wave-induced rotors. *J. Atmos. Sci.*, **59**, 186-201

Haimov, S., V. Grubišić, J. French, and L. Oolman, 2008: Multi-Doppler measurements of atmospheric rotors and turbulent mountain waves. IEEE IGARSS Symposium, Boston, MA.

Retrieval and application of raindrop size distributions from polarimetric radar data for sub-synoptic scale systems

Petar Bukovcic*, ***, ****, Dusan Zrnic**, and Guifu Zhang***, ****

*Cooperative Institute for Mesoscale Meteorological Studies, University of Oklahoma, and NOAA/OAR National Severe Storms Laboratory, Norman, Okalhoma
**National Severe Storms Laboratory, NOAA, Norman, Oklahoma
***School of Meteorology, University of Oklahoma, Norman, Oklahoma
****Atmospheric Radar Research Center, University of Oklahoma, Norman, Oklahoma

1. Introduction

Polarimetric radars measure reflectivity at horizontal and vertical polarization, differential reflectivity, specific differential phase, and copolar cross correlation coefficient that depend on cloud/precipitation physics (Cao et al., 2008; Zhang et al., 2001; Zrnic and Ryzhkov, 1999). These measurements provide information about hydrometeor size, shape, orientation and phase, and allow for the retrieval of rain drop size distributions (DSDs). The radar measurements and retrivals have the potential to improve model microphysical parametrization and quantitative precipitation forecast. A 2-dimensional video disdrometer (2DVD) directly measures the shape, size and falling velocity of precipitation particles, which is essential for verifying and interpreting polarization radar data.

2. Datasets

Datasets for three mesoscale events, convective-stratiform mix on June 26 2007, convective storm on June 28 2007 and squall-line event on May 13 2005, were collected with S-band polarimetric weather radar (KOUN) and OU 2DVD. Radar data at the disdrometer location is an average of a 2x5 (azimuth x range-gates) box of resolution volumes from the 0.5 degree elevation scan, centered on the volume located above the location of the disdrometer. The range gate spacing is 0.25 km. The disdrometer measured DSDs are sampled for 1-minute duration. For the May 13 2005 case, the disdrometer was deployed at approximately 29 km south from KOUN. Regarding the other two events, June 26 and June 28 2007, 2DVD was located approximately 65 km southwest from KOUN.

3. Methodology

Fundamental information associated with rain microphysics is contained in rain drop size distribution (DSD). Gamma distribution, $N(D) = N_0 D^{\mu} \exp(-\Lambda D)$, has been widely accepted to model rain DSDs in recent years (Zhang et al., 2001; Brandes et al., 2004). Using the constraining relation where shape parameter $\mu = -\ 0.0201\Lambda^2 + 0.902\ \Lambda - 1.718$ (Cao et al., 2008), gamma DSD model reduces to a two-parameter model whose parameters N_0 and Λ can be retrieved from the radar measured reflectivity at horizontal polarization Z_H, and differential reflectivity Z_{DR} (Zhang et al. 2001).

4. Case studies

Several sub-synoptic/mesoscale events have been studied: a convective-stratiform mix on June 26 2007, a convective storm on June 28 2007, and a squall-line case on May 13 2005. Due to page limit, only one example is shown in Fig. 1.

The June 26 event started about 0700 UTC with light convective rain at the disdrometer site. In the beginning stage, storm was convective (from 0700-1100 UTC), while subsequent periods were mainly stratiform. Storm motion relative to the 2DVD and KOUN was from southwest to northeast.

Vertical profile time evolution over the disdrometer site of radar variables Z_H, Z_{DR} and ρ_{hv} is shown in Fig. 1, left panel. In the initial stage, several convective cells developed (from 0700-1100

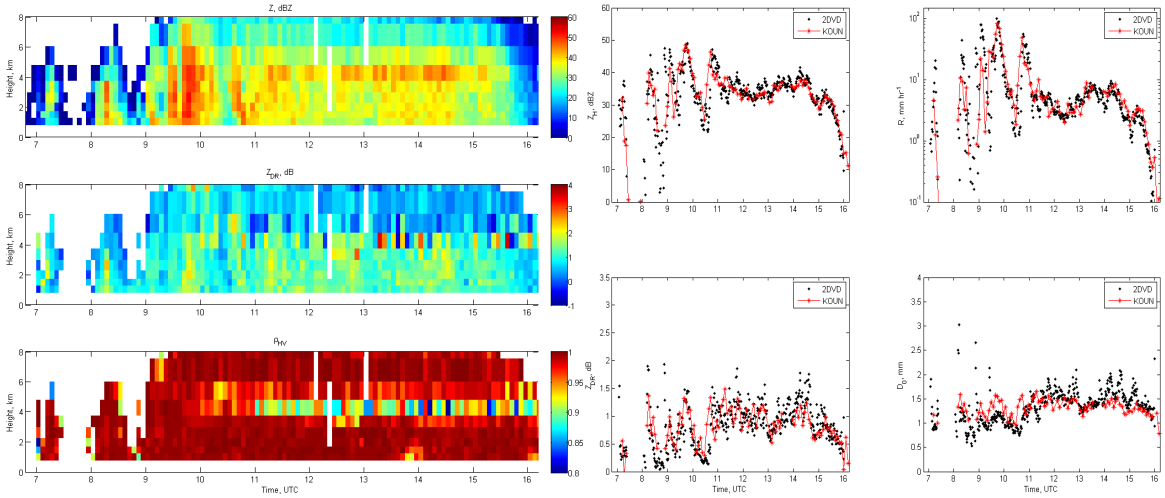

Figure 1. Left panel: Height-time evolution of vertical profiles of Z_H [dBZ], Z_{DR} [dB] and ρ_{HV} (top to bottom, respectively) measured with KOUN at 2DVD site; Right panel: Comparison of Z_H [dBZ] (top left), Z_{DR} [dB] (bottom left), rainfall rate R [mm/hr] (top right), and median volume diameter D_0 [mm] (bottom right) obtained from radar DSD retrieval (KOUN, red line with asterisks) and disdrometer (black dots), time series, 0.5° KOUN elevation angle.

UTC), with the most distinctive one from 0930 to 1010 UTC with high Z_H values reaching the height of 8 km. Bright band signature is clearly seen in stratiform period of the storm from 1120 to 1530 UTC at height of ~ 4km.

Comparisons between radar Z_H, Z_{DR}, DSD retrieved microphysical parameters rainfall rate R and median volume diameter D_0 with 2DVD measurements are shown in Fig. 1, right panel. Radar retrieved median volume diameter is slightly overestimated for convective part and slightly underestimated for stratiform part of the storm in comparison to the 2DVD values. Radar estimation of rainfall rate is in fair agreement for convective part and in very good agreement for stratiform stage of the storm. Similar results are retrieved for the other two events.

5. Conclusions

Observations and data analysis of mesoscale rain events collected with S-band polarimetric KOUN radar and a 2DVD in central Oklahoma are presented. The DSD retrievals from radar measurements are in good agreement overall with disdrometer counterparts, although there were some discrepancies. A better understanding of rain microphysical properties, along with reliable retrieval technique, is essential for accurate rain estimation and model parameterization.

References

Brandes, E. A., G. Zhang, and J. Vivekanandan, 2004: Drop size distribution retrieval with polarimetric radar: model and application. *J. Appl. Meteor.,* **43**, 461-475

Cao, Q., G. Zhang, E. Brandes, T. Schuur, A. Ryzhkov, and K. Ikeda, 2008: Analysis of video disdrometer and polarimetric radar data to characterize rain microphysics in Oklahoma. *J. Appl. Meteor. Climat.* **47**, 2238-2255

Zhang, G., J. Vivekanandan, and E. Brandes, 2001: A method for estimating rain rate and drop size distribution from polarimetric radar. *IEEE Trans. Geosci. Remote Sensing,* vol. **39**, No.4, 830-840.

Zrnic, D. S. and A. V. Ryzhkov, 1999: Polarimetry for weather sur veillance radars. *Bull. Amer. Meteor. Soc.*, **80,** 389-406.

Polarimetric Radar Observations of Hydrometeor Refreezing in Winter Storms

Matthew R. Kumjian*, Alexander V. Ryzhkov*, Terry J. Schuur*, and Heather D. Reeves**

*Cooperative Institute for Mesoscale Meteorological Studies, University of Oklahoma, Norman, Oklahoma, USA

**National Severe Storms Laboratory, Norman, Oklahoma, USA

1. Introduction

Winter precipitation events, especially those involving transitions of precipitation type, continue to pose a formidable forecasting and nowcasting challenge to operational meteorologists. Small changes in environmental thermodynamic conditions can alter the precipitation type observed at the ground, and conventional single-polarization radar data are insufficient for distinguishing between various hydrometeors. However, with the advent of dual-polarization radars, such identification of hydrometeor types is possible, providing meteorologists with information about the precipitation physics and particle types present in winter storms.

Recent investigations of winter storm datasets collected by polarimetric radars operating at S, C, and X bands reveal certain repetitive signatures related to the ongoing microphysical processes in such storms (Kumjian et al. 2011). One of these signatures is a newly-observed low-level enhancement of the differential reflectivity factor (Z_{DR}) seemingly associated with the refreezing of melted or partially-melted hydrometeors (Fig. 1). In this study, observations of this refreezing signature are presented, with data from several winter storm cases shown.

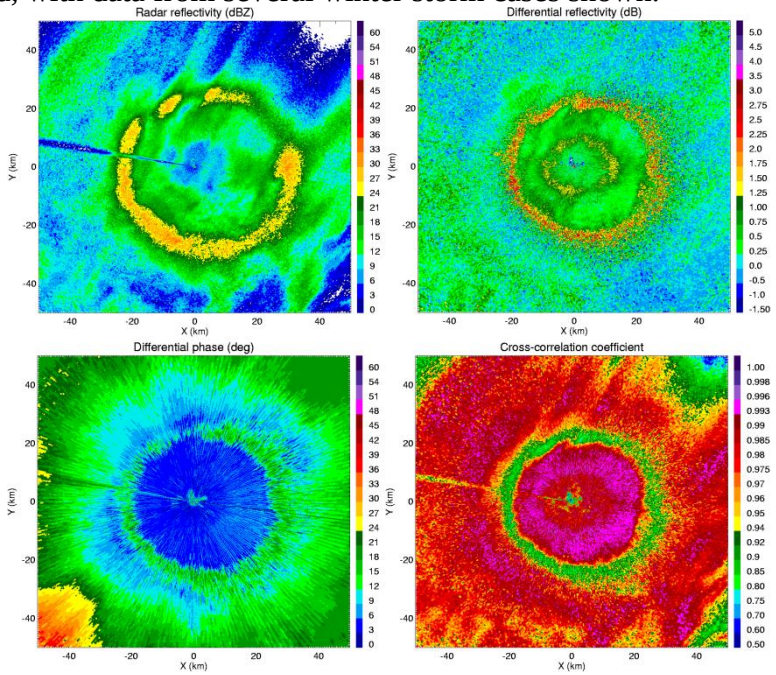

Figure 1. Observations from the C-band OU-PRIME radar from 1641 UTC on 24 December 2009, taken at 3.4° elevation. Fields are Z_H (top left), Z_{DR} (top right), Φ_{DP} (bottom left), and ρ_{hv} (bottom right). The refreezing signature is the inner "ring" of enhanced Z_{DR}.

2. Approach

For each case the refreezing signature is first identified using displays of the polarimetric radar variables (reflectivity factor at horizontal polarization Z_H, Z_{DR}, specific differential phase K_{DP}, and co-polar cross-correlation coefficient ρ_{hv}) obtained from PPI scans (Fig. 1). The signature is evident

as a circular (or, partial circle) enhancement of Z_{DR} beneath the melting layer bright band, the latter of which is evident as a pronounced increase in Z_H, Z_{DR}, K_{DP}, and a decrease in ρ_{hv}. Once a refreezing signature is identified, "quasi-vertical profiles" of the polarimetric radar variables (Fig. 2) are constructed from the constant-elevation PPI scans. This is done by first taking azimuthal medians of each variable over a homogeneous sector. Then, the slant range is converted to height AGL following Doviak and Zrnić (1993). If available and representative of the environment, radiosonde observations from Norman are compared to the reconstructed vertical profiles of the radar variables.

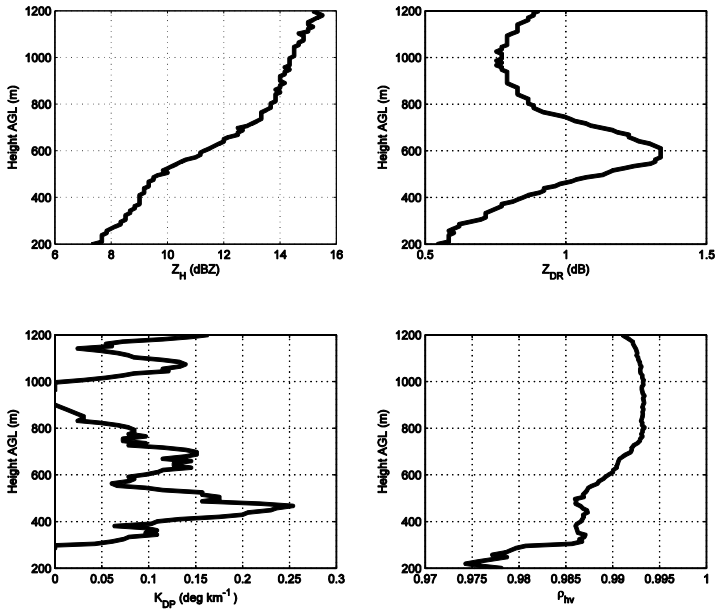

Figure 2. Quasi-vertical profiles of the polarimetric variables from the time of observations in Fig. 1.

3. Discussion

In each of the 5 cases observed so far, the signature appeared as the surface precipitation type transitioned from freezing rain to ice pellets. In such a transition from liquid to ice, a decrease in Z_{DR} is expected owing to a decrease in particle refractive index. In fact, the opposite (increase in Z_{DR}) occurs, implying the generation of anisotropic particles, presumably ice crystals. The signature is consistently found at an altitude just beneath the low-level temperature inversion, with air temperatures < -5 °C and subsaturated (with respect to water) conditions present. Such conditions are favorable for rapid depositional growth of needle-like (i.e., very anisotropic) crystals. However, it is unclear what *generates* the ice crystals. Two plausible explanations include (i) activation of ice nuclei when temperatures become sufficiently cold (< -5 °C), and (ii) shattering of particles undergoing freezing; the resultant splinters then rapidly grow in the ice-supersaturated conditions. Ongoing modeling efforts will help test these hypotheses. The ice mass content can be estimated from K_{DP} following Ryzhkov et al. (1998), providing evidence for the quantity of anisotropic ice crystals generated concurrently with the refreezing of raindrops into ice pellets.

References

Doviak, R.J., and D.S. Zrnić, 1993: *Doppler Radar and Weather Observations*, 2nd ed. Dover Publications, New York, 562 pp.

Kumjian, M.R., H.D. Reeves, and A.V. Ryzhkov, 2011: Polarimetric signatures in winter storms. *NOAA/NSSL Report*, 27 pp.

Ryzhkov, A.V., D.S. Zrnić, and B.A. Gordon, 1998: Polarimetric method for ice water content determination. *J. Appl. Meteor.*, **37**, 125-134.

Impact of the large-scale wind and mesoscale shallow flows on the development of cumulonimbus clouds over Istria

Gabrijela Poljak*, Karmen Babić**, Marko Kvakić**, and Maja Telišman Prtenjak**

** Primary School "Tenja", Osijek*
*** Andrija Mohorovičić Geophysical Institute, Department of Geophysics, Faculty of Science, University of Zagreb, Zagreb, Croatia*

1. Introduction

Thermally-induced flows, such as sea/land breezes (SLB), influenced by complex topography are very common along the Mediterranean coast. They have been extensively studied in different Mediterranean regions exhibiting at the same time theirs relationship with a particular cloud type and convection (e.g. Azorin-Molina et al. 2009, Babić et al. 2012). The inland SB penetration can be traced by the cumulus type of clouds in satellite images. Occasionally, the cumulus clouds developed into a cumulonimbus (Cb) clouds that caused thunderstorm and rainfall over the local area (Miller et al. 2003).

Recently, over the northeastern Mediterranean region, the focus was on the relative long-term analysis of the available lightning data (Mikuš et al. 2012) as a measure of convection and on the possible relationship between SB and Cb clouds during summer months (Babić et al. 2012). Mikuš et al. (2012) detected 402 convective days in the warm part of the period of 2006-2009 and showed some characteristics of convective activity along the Adriatic coast and over the open sea. The northeastern (NE) Adriatic, in particular, the Istrian peninsula, represents the most convective area in Croatia with 62.4% of all days in the sample. The peak in *daytime* convective activity during almost *non-gradient pressure field* existed in July followed by the slightly lower activity in June. In 82% of overall days with convective activity above NE Adriatic was observed during three dominant wind regimes on a large scale: from SW (46%), NE (18%) and NW (18%) directions.

The determination of the relationship between SB at the coastal stations and Cb over Istria for a 10-year period (1997-2006) showed that in 51 % of daytime Cb days, SB develops along the coast (Babić et al. 2012). The results have revealed the most frequent conditions during the Cb clouds generation. For example, the temperature difference between land and sea is in the range of 3 and 5 °C and the maximum SB speed at the coast is in the range of 3 and 5 m s^{-1}.

Therefore, according to the results of the above observational (more "climatological") studies, the aim is to estimate in a more detail a possible influence of the jointed large scale wind and thermally-induced local wind on the Cb development over Istria. Results are based on the numerical mesoscale model that will supplement the lower spatial and temporal coverage of measurements of both phenomena.

2. Description of simulations

Here we selected and simulated three chosen cases from the dataset of Babić et al. (2012) that satisfy simultaneous occurrence of SB and daytime Cb above Istria (Table 1). An each selected case also contains an interaction of SB with one of the dominant types of large-scale wind (SW, NE, NW) above Istria. The simulations were performed by the WRF-ARW mesoscale model with: ECMWF input and boundary data, a two-way nesting, a Lambert conformal projection, 3 domains with 1.5 km grid spacing in the finest domain (Fig. 1) and 70 vertical levels.

Table 1. Three selected simulated WRF cases with the Cb cloud over Istria in which the SB interact with one of the dominant types of large-scale wind (SW, NE, NW). Both the SB duration and speed were evaluated at the Pula-airport site (tip of the Istria peninsula).

	date	Dominant large-scale wind	Cb duration onset – end (CET)	SB duration onset – end (CET)	Max SB speed
Case A	09 July 2006	NE	10:50 – 16:00	9- 19	5.1
Case B	08 June 2003	SW	12:40 - 16:30	9- 20	3.6
Case C	08 August 2006	NW	11:10 – 16:30	9- 13	4.1

3. Results and discussion

According to WRF results, the interaction between local SB and large-scale wind significantly influenced the position of the Cb development (Fig. 1). The large-scale NE wind simultaneously enhanced the SB at the southeastern Istrian coast and prevented deeper penetration of the dominant western SB over the peninsula (within 15 km, Fig. 1a). The interaction reinforces the convergence of the flow field in the boundary layer and consequently the intensity of SB fronts and its updrafts. Results (Fig. 1b) indicate that the SW large-scale wind interacts with the western SB allowing deeper inland penetration over the peninsula (> 30 km) than in Case A. The Cb development was associated with the position of the convergence in the wind field. The large-scale NW wind (Fig. 1c) was superimposed on the western SB producing larger inland penetration and amplifying the magnitude of the SB speed. Still, the spatial position of the convergence zone caused by the NW wind and Istrian SBs was strongly curved. In all three cases, a significant amount of cloudiness and certain amount of precipitation have been developed in the zone of the convergence between 11 UTC and 13 UTC and moved depending on the type of the large-scale wind southward (in Cases A, C) or northward (in Case B) of the peninsula.

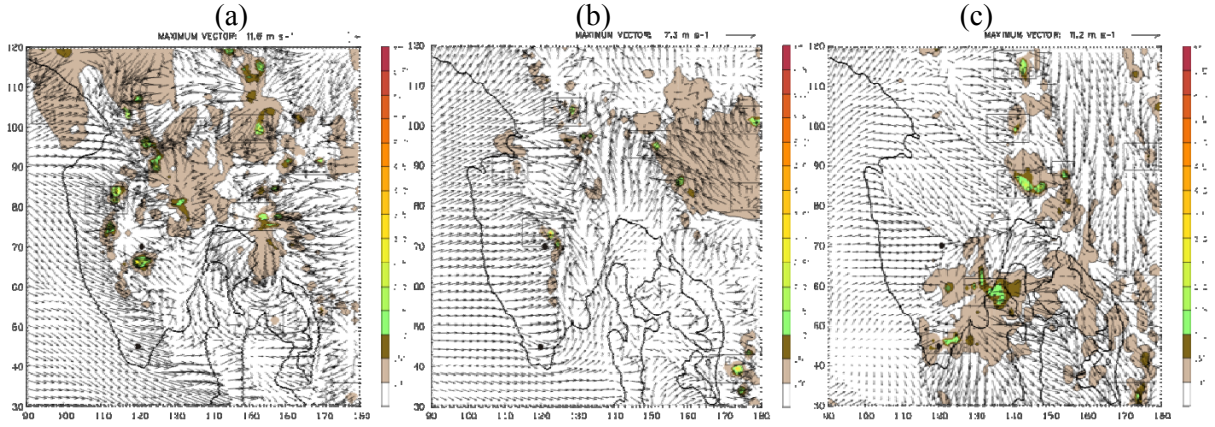

Figure 1. A close up of the WRF-ARW modeled results (10-m wind and column-integrated cloud hydrometeors) at 14 CET in the finest model domain, Δx =1.5 km obtained for: (a) Case A, (b) Case (B) and (c) Case C.

References

Azorin-Molina, C., A. Sanchez-Lorenzo, and J. Calbo, 2009: A climatological study of sea breeze clouds in the southeast of the Iberian Peninsula (Alicante, Spain). *Atmosfera*, **22**, 33–49.

Babić, K., P. Mikuš, and M. T. Prtenjak, 2012: The relationship between shallow thermal circulation regimes and cumulonimbus clouds along northeastern Adriatic coast. *Geofizika*, (in press).

Miller, S. T. K., B. D. Keim, R. W. Talbot, and H. Mao, 2003: Sea breeze: Structure, forecasting, and impacts. *Rev. Geophys.*, **41**, No. 1011. DOI: 10.1029/2003RG000124.

Mikuš, P., M.T. Prtenjak, and N. Strelec Mahović, 2012. Analysis of the convective activity and its synoptic background over Croatia. *Atmos. Res.*, **104/105**, 139-153.

Covariance localization for convective-scale EnKF

Ryan A. Sobash* and David J. Stensrud**

*School of Meteorology and Cooperative Institute for Mesoscale Meteorological Studies, University of Oklahoma
**NOAA/OAR/National Severe Storms Laboratory

1. Introduction

Covariance localization is a ubiquitous trait of high-dimensional EnKF data assimilation experiments, where the ensemble size is constrained by available computing resources. Localization attempts to remove spurious covariances dominated by sampling noise, while retaining the meaningful, flow-dependent covariances. Common localization choices use a distance-dependent weighting function, forcing covariances to zero beyond a specified cutoff distance. The proper choice of this cutoff is a complex function of ensemble size, observation density, type, location, and the underlying system dynamics. Most previous studies differ in their experimental design, preventing robust conclusions about a proper choice of localization for EnKF studies assimilating WSR-88D radar datasets. To further understand the sensitivities of covariance localization on EnKF analyses of convective systems, this study investigated several OSSEs of a developing convective system, using localization cutoff choices spanning the range chosen in previous work.

2. Model simulations

The Advanced Research Weather Research and Forecasting (WRF-ARW) model (Skamarock et al. 2005) V3.2.1 was used to create a truth simulation of a developing MCS. Convection was triggered with 5 +3K bubbles, with random perturbations added along the bubble edges to initiate three-dimensional motions (Fig. 1). The WRF-ARW was integrated as a cloud-model with WRF 6-class single-moment (WSM6) microphysics, open-boundary conditions, no terrain, surface physics, or boundary-layer physics. Synthetic radial velocity and reflectivity observations were extracted from the truth simulation every five minutes assuming a radar placement at the center of the domain. Observation errors were added to each observation by performing a random draw from a Gaussian with zero mean and standard deviation of 2 m s^{-1} (2 dBZ) for radial velocity (reflectivity). Reflectivity observations of less than 10 dBZ were considered "clear-air" observations for the purposes of this study and the corresponding radial velocity observation at these locations was removed. All other observations are considered "precipitation" observations.

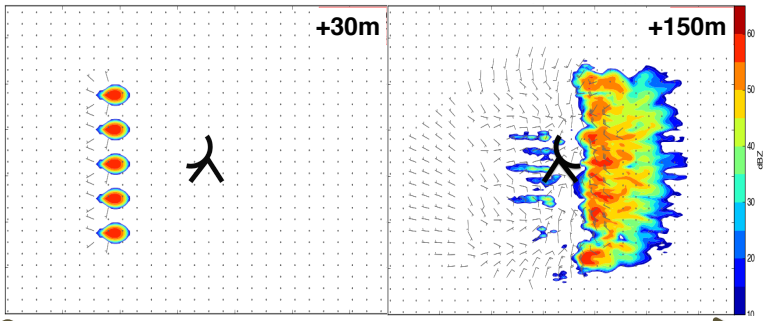

Figure 1. Truth simulation at the (left) beginning and (right) end of the assimilation period.

3. Assimilation experiments

For all the OSSEs, a 50-member ensemble was constructed by adding random, uncorrelated Gaussian noise to the wind profiles of the truth sounding. The OSSEs were initialized 30-minutes after the beginning of the truth simulation when appreciable amounts of hydrometeors develop

within the simulated storm. The synthetic observations were assimilated every 5-minutes for 150 minutes. Additive noise (Dowell et al. 2009) was used to maintain ensemble spread. The OSSEs are identical except for the localization cutoffs (r) and choices for the horizontal observation data spacing. Values of 6, 12, and 18 km are selected for r ($r_h = r_v$), along with 1 and 2 dx for the horizontal data spacing of the precipitation observations. The localization choices for the clear-air observations remain constant across all experiments; those observations are thinned to 2 dx with r = 12 km.

4. Results and Discussion

Changes in the covariance localization produce analyses with different error characteristics (Fig. 2). Overall, the 12 km localization experiment produces analyses with smaller RMSE for most of the state variables. In addition, the optimal localization length is shown to vary with time, as the simulated convective system grows upscale. During a period of cell mergers, the 18 km localization experiment produces analyses with the smallest RMSE. To further understand these differences, correlations between the assimilated observations and state variables were computed to determine typical correlation length scales for each obs-state pair. The length scales are smaller for the microphysical variables than the three-dimensional wind field, although both length scales increase as the convective system grows upscale (not shown). Together, these results demonstrate a significant need for adaptive localization methods in convective-scale EnKF.

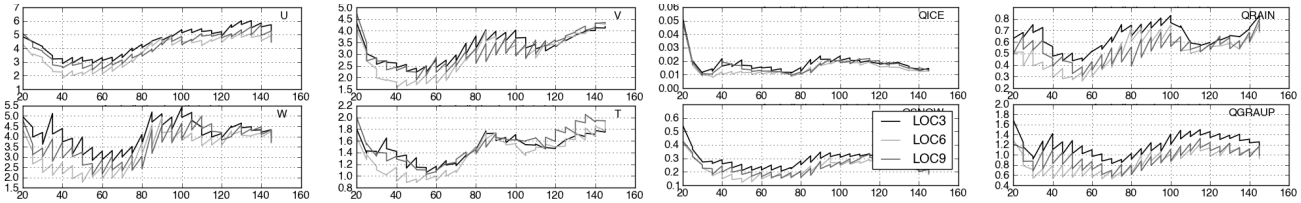

Figure 2. Ensemble mean RMSE for 8 state fields during the 150 minute assimilation period.

The localization sensitivity results herein suggests that when assimilating radar data with the temporal and spatial resolution typically provided by a WSR-88D, a larger horizontal (~12 km), but smaller vertical (~3 km) localization cutoff (using a typical Gaspari-Cohn localization function) than previous studies could be beneficial, especially in cases where the convective evolution is dominated by thunderstorms interactions, mergers, and/or upscale growth into a linear convective system. Previous convective-scale enKF studies (e.g. those summarized in the introduction), employing both OSSEs and real-data experiments, primarily have focused on an individual thunderstorm cell (e.g. tornadic supercells). While these studies have laid the foundation for convective-scale enKF and proved its viability, the scenarios depicted in these studies are only a subset of the large variety of convective modes observed in nature. Thus, more work is needed to demonstrate how those results generalize to other types of convective systems and severe weather hazards (e.g. large surface winds). The work herein begins to explore these inherently more complex convective systems.

References

Dowell, D. C., and L. J. Wicker, 2009: Additive Noise for Storm-Scale Ensemble Data Assimilation. *J. Atmos. Oceanic Technol.*, **26**, 911–927.

Skamarock, W. C., J. B. Klemp, J. Dudhia, D. O. Gill, D. M. Barker, W. Wang and J. G. Powers, A Description of the Advanced Research WRF Version 2, NCAR Technical Note, 2005.

Tong, M., and M. Xue, 2005: Ensemble Kalman Filter Assimilation of Doppler Radar Data with a Compressible Nonhydrostatic Model: OSS Experiments. *Mon. Wea. Rev.*, **133**, 1789–1807.

Analysis of convective indices over the northeastern Adriatic

Karmen Babić*, Gabrijela Poljak**, Marko Kvakić*, and Maja Telišman Prtenjak*

** Andrija Mohorovičić Geophysical Institute, Department of Geophysics, Faculty of Science, University of Zagreb, Zagreb, Croatia*
*** Primary School "Tenja", Osijek*

1. Introduction

The northeastern (NE) Adriatic represents the most convective area in Croatia, particularly the Istria, with more than 60% of convective days in the warm part of the years 2006-2009 (Mikuš et al. 2012). This area has a maximum number of convective days later in summer, mostly in August. However, the June-to-August variation in a number of selected convective days along the northeastern Croatian coastline was rather small. It also corresponds very well to the monthly thunder day distribution along the adjacent northern Italian Adriatic coast (Manzato, 2007). Mikuš et al. (2012) obtained that three dominant wind regimes on a large scale were observed in 82% of overall days with convective activity above NE Adriatic. They were from the SW (46%), NE (18%) and NW (18%) directions. Furthermore, the non-gradient pressure (NG) field (21%) is a dominant summer large-scale weather type with a maximum in July. The center of the cyclone (C, 21%), the eastern front sector of the cyclone (20%), the western back side of the cyclone (10%) and the front side of the trough (T, 12%) are the most common weather types in spring and late summer-autumn periods.

Thermally-induced flows, such as sea breeze (SB), are also very common phenomena along the Croatian coast (Babić et al. 2012) occurring on the average in 50 % of all summer days. Due to relatively large frequency of occurrence of both SB and cumulonimbus (Cb) clouds, their relationship was recently investigated. The results have revealed that in 51 % of daytime Cb occurrence, SB develops along the coast (Babić et al. 2012). However, the determination of theirs relationship is still based only on the surface measurements of two measuring sites, not allowing a deeper temporal and spatial analysis of their interaction (and characteristics of deep moist convection) over Istria.

2. Average characteristics of the convective indices for NE Adriatic region

Based on the dataset of convective days for the NE Adriatic region in Mikuš et al. (2012), we determined instability indices from the Udine (46.03°N, 13.18°E) radiosounding site which is the only radiosounding station in that part of the Adriatic coast. According to Groenemeijer and van Delden (2007) soundings within 100 km of the storm's event can satisfactory describe deep moist convective conditions. The mean values and standard deviations of the convective available potential energy (CAPE), convective inhibition (CIN), lifted index (LI), K-index (KI) and Bulk Richardson number (RiB) are presented in Table 1, showing some numerically convective characteristics of the dominant weather type and wind regime in NE Adriatic region.

Table 1. Mean values of convective available potential energy (*CAPE*, J/kg), convective inhibition (*CIN,* J/kg), Lifted index (*LI*, K), K-index (*KI*, K) and Bulk Richardson number (RiB) and their standard deviations for Udine radiosounding station. Abbreviations are: NG = non-gradient pressure field, C = cyclone, T = trough.

		$\overline{(CAPE)} \pm \sigma$	$\overline{(CIN)} \pm \sigma$	$\overline{(LI)} \pm \sigma$	$\overline{(RiB)} \pm \sigma$	$\overline{(KI)} \pm \sigma$
weather type	NG	428.7 ± 438.6	-71.5 ± 95.7	**-1.0** ± 2.3	77.7 ± 140.8	29.0 ± 4.9
	C	230.5 ± 351.2	-68.5 ± 65.9	0.8 ± 2.7	32.9 ± 97.4	27.2 ± 5.8
	T	**507.5** ± 575.1	-72.5 ± 59.7	-0.5 ± 3.2	**84.5** ± 202.4	29.8 ± 6.0
large-scale wind	SW	332.2 ± 490.6	-74.2 ± 67.8	0.4 ± 3.0	50.4 ± 236.3	28.8 ± 5.3
	NE	237.4 ± 327.3	-70.3 ± 63.1	-0.1 ± 2.1	31.8± 85.1	27.2 ± 6.4
	NW	**529.6** ± 629.0	-47.9 ± 100.5	**-0.2** ± 3.6	**146.8** ± 260.1	27.8 ± 8.3

The high mean values of CAPE and the KI and a negative LI correspond to the trough and non-gradient pressure field weather types that dominate during summer months. Lower values of the same indices are found for the cyclonic type due to its seasonal occurrence in spring and autumn. RiB has the lowest value for C weather type and much higher values for T and in days with the NG weather type. These large values due to lack of shear, suggest a high potential for ordinary or multicell storm development. Values of RiB being lower than 45 for the T weather type and for the SW flow regime, suggest conditions favorable for supercell development. The NW wind regime is followed by the highest atmospheric instability (smallest CIN and highest CAPE, LI and RiB) and the NE wind regime is accompanied by the lowest atmospheric instability.

3. Results and discussion of numerical simulations

In order to get insight into the spatial and temporal distribution of convective parameters we selected and simulated three chosen cases from the dataset of Babić et al. (2012) that satisfy simultaneous occurrence of SB and daytime Cb above Istria. An each selected case also contains an interaction of SB with one of the dominant types of large-scale wind: NE, SW and NW above Istria. The simulations were performed by the WRF-ARW mesoscale model. To evaluate the influence of the SB over the Istria on the moist convection processes and convective indices, we performed an additional numerical sensitivity test for the case with NE large-scale wind without microphysics scheme (called A0 case).

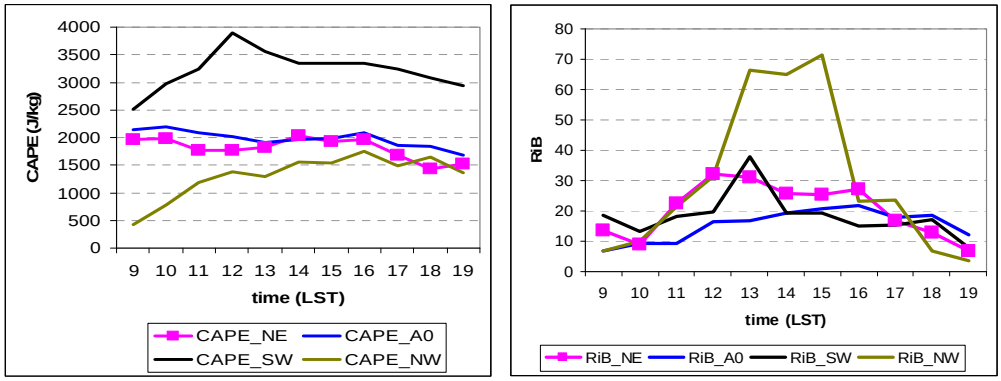

Figure 1. Temporal evolution of max *CAPE* (J/kg) and max RiB above Istria from three selected simulated WRF cases covering dominant types of large-scale wind (SW, NE, NW).

Results (Fig. 1) showed only partial similarities with average convective indices in Udine. Opposite to the "climatological" relationship between CAPE and wind regimes, the most prominent CAPE values are for the superposition of SW large-scale and the SB flow. They are however accompanied by the relative small RiB (< 45), Fig. 1. As we expected, the NW case has the largest RiB (> 60) that coincides with values in Table 1.

References

Babić, K., P. Mikuš, and M. T. Prtenjak, 2012: The relationship between shallow thermal circulation regimes and cumulonimbus clouds along northeastern Adriatic coast. *Geofizika*, (in press).

Groenemeijer, P.H., and A. van Delden, 2007: Sounding-derived parameters associated with large hail and tornadoes in The Netherlands. *Atmos. Res*. **83**, 473–487.

Mikuš, P., M.T. Prtenjak, and N. Strelec Mahović, 2012: Analysis of the convective activity and its synoptic background over Croatia. *Atmos. Res.*, **104/105**, 139-153.

Manzato, A., 2007: The 6 h climatology of thunderstorms and rainfalls in the Friuli Venezia Giulia Plain. *Atmos. Res*. **83**, 336–348.

Satellite-based overshooting tops detection methods: comparison and validation

Petra Mikuš*, and Nataša Strelec Mahović*
Meteorological and Hydrological Service, Grič 3, Zagreb, Croatia

1. Introduction

Detection and possible nowcasting of severe convective storms is one of the most challenging tasks for operational forecasters. Several studies showed that severe thunderstorms show specific signatures or shapes in the thunderstorm cloud tops, such as cold rings and cold-U/V signatures (e.g. Setvak et al., 2007) as well as the overshooting tops (OT) (e.g. Bedka, 2010). OTs can be most easily identified in the high-resolution visible channel imagery as the lumpy textured appearance, however only during day-time. In the 10.8 μm infra-red window (IRW) channel, available during both day and night, a small cluster of very cold brightness temperatures can indicate that an OT is present. Other studies have combined IRW channel temperatures with those from the 6.2 μm water vapor (WV) absorption channel to identify OTs. Both IRW-only and WV-IRW techniques have shown some disadvantages when used alone, so it is important to evaluate the information provided by other spectral channels in an effort to improve objective OT detection. Here we use data from the SEVIRI imager on-board the Meteosat Second Generation (MSG) satellites to test four OT detection methods that use combinations of SEVIRI channels in the form of channel differences.

2. Satellite-based OT detection methods

Satellite based methods for the detection of convective clouds and the heights of their tops are usually based on IRW measurements. One of the most commonly used methods for detecting OTs is based on the brightness temperature difference (BTD) between the 6.2 μm and 10.8 μm (WV-IRW) channels. WV-IRW BTD greater that 0 K indicates presence of deep convective clouds and OTs. According to Kwon et al. (2010) BTD of the ozone channel (9.7 μm) and the IRW channel also shows positive signature for the cloud tops above 11 km. They pointed out that the signal of BTD between ozone and IRW channel is even more significant than BTD WV-IRW near the tropopause suggesting that it could be a better indicator for the deep convective activity than BTD of WV and IRW channels. Additionally, BTD of carbon dioxide (13.4 μm) and IRW channel can also be used for determining the height of the opaque clouds. The reason is that with higher cloud tops the absorption effect of CO2 gets smaller, making the BTD of the CO2 and IRW channel close to 0 or positive, in case of very deep convective clouds.

Table 1: The IRW brightness temperature and the BTD thresholds for the WV-IRW, CO2-IRW, O3-IRW and COMB BTD method.

BTD	**Threshold**	
WV-IRW	IRW brightness temperature < 215 K	> 4 K
CO2-IRW		> 3.5 K
O3-IRW		> 13 K
COMB		> 4 K & > 13 K

All methods presented in our study include two criteria: one for the IRW brightness temperature and the other for BTD (Table 1). The COMB BTD method, a combination of BTD O3-IRW and WV-IRW includes IR brightness temperature criteria and the criteria for both BTDs.

3. Comparison of the methods

Overshooting tops detected using the studied BTD methods are shown using the example of a convective system seen in color-enhanced Meteosat 9 10.8 μm channel image at 16:45 UTC, on 23 July 2009 (Fig. 1a). Region of deep convective clouds, recognizable in the color-enhanced IR image as orange-red colored pixels, is located above north Austria and south of the Czech Republic. Brightness temperature of the coldest cloud tops is lower than 205 K (dark red in Fig. 1a) meeting the criteria for 10.8 μm BT mentioned in Table 1. The BTD fields for studied case are shown in Figs. 1c to 1f. In general, all four methods show good correspondence of the detected pixels with deep convective clouds.

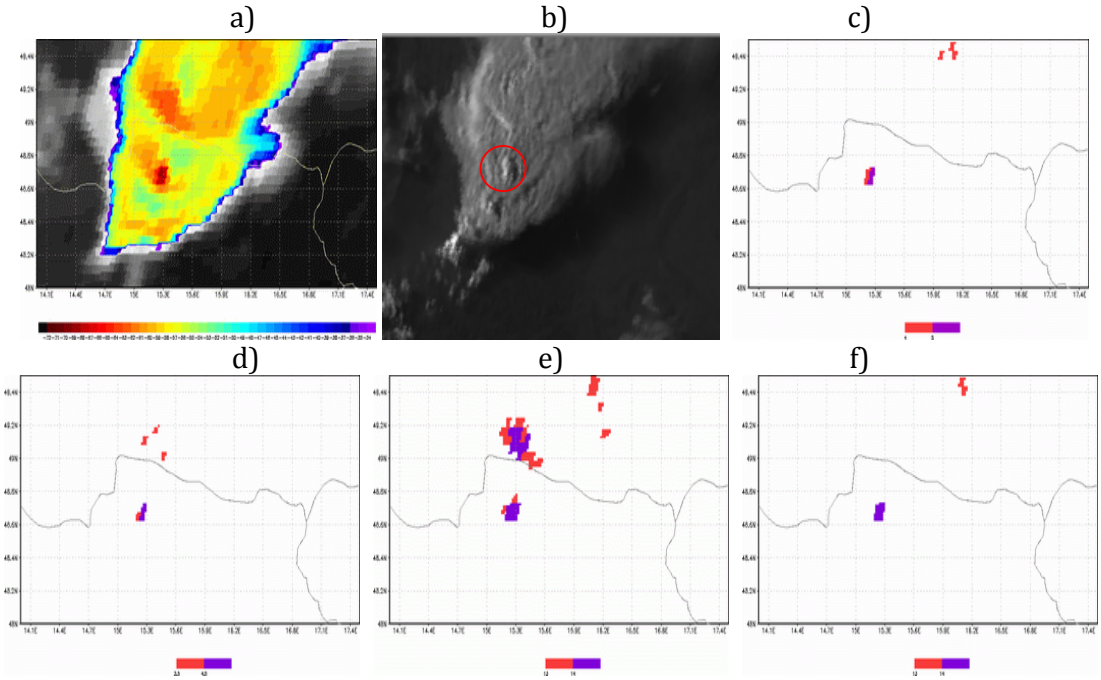

Figure 1: a) Color-enhanced Meteosat 9 10.8 (IRW) μm image at 16:45 UTC, 23 July 2009. Color scale from -33°C (purple) to -72°C (dark red). b) Meteosat 9 HRV channel image. Location of observed OT is marked with the red cycle. Location of pixels meeting the criteria for the brightness temperature and brightness temperature difference, detected using c) WV–IRW, d) CO2–IRW, e) O3-IRW and f) COMB BTD method.

4. Conclusion

We can conclude that all four investigated BTD methods indicate deep and very intense convection but not necessarily the OTs. In most cases pixels meeting defined criteria are too widely dispersed to exclusively represent OTs. The most of the OT pixels referred to as “false alarm”, are located within the specific signatures or shapes, such as cold ring or cold U/V, in the severe thunderstorm cloud tops.

References

Bedka, K. M., 2010: Overshooting cloud top detections using MSG SEVIRI Infrared brightness temperatures and their relationship to severe weather over Europe. *Atmos. Res.,* doi:10.1016/j.atmosres.2010.10.001.

Setvak, M., R. M. Rabin, and P. K. Wang, 2007: Contribution of the MODIS instrument to observations of deep convective storms and stratospheric moisture detection in GOES and MSG imagery. *Atmos. Res.*, **83**, 505-518.

Kwon, E. H., B. J. Sohn, J. Schmetz, and P. Watts, 2009: Use of ozone channel measurements for deep convective cloud height retrievals over the tropics. *16th Conference on Satellite Meteorology and Oceanography*, 11-15 January, 2009, Phoenix, AZ, USA.

Observational Analysis of a Gravity Wave Traversing Oklahoma on April 26, 2011

Timothy A. Bonin* and Phillip B. Chilson*

**Atmospheric Radar Research Center and School of Meteorology, University of Oklahoma, Norman, OK, USA*

1. Introduction

For several decades, gravity wave case studies have been conducted to better understand the influence of gravity waves on the weather. Gravity waves can affect various thermodynamic and dynamic fields (Bosart and Sanders 1986). Additionally, gravity waves are capable of triggering convection and modifying cloud cover (Pothecary 1954).

On the afternoon of April 26, 2011 an apparent gravity wave from southwestern Oklahoma was observed by numerous instruments as it propagated to the northeast. With the wave's passing, winds shifted and cloudiness was altered significantly. Additionally, Oklahoma Mesonet stations recorded a pressure fluctuation associated with this event. In northeastern Oklahoma, a severe storm was initiated in the vicinity of the gravity wave.

2. Instrumentation

Three different instruments were used to examine the characteristics of the passing gravity wave. Surface pressure and wind speed measurements from various Oklahoma Mesonet sites provided propagation path and intensity of the gravity wave. The Oklahoma Mesonet consists of 110 sites throughout the state that measure air tempreture, humidity, barometric pressure, wind speed and direction, and surface and subsurface conditions (McPherson et al. 2007).

At the time of the event, a Metek PCS.2000-16 Doppler sodar was installed very close to the National Weather Center (NWC) in Norman, OK. The sodar provides 10 minute averaged measurements for each of the three components of the wind, along with standard deviations of each component. It provides 10 m vertical resolution, with the lowest sampling volume located 20 m above ground level (AGL). The maximum height depends on atmospheric conditions.

During the time of the gravity wave passage, the Small Multifunction Autonomous Research and Teaching Sonde (SMARTSonde), a small unmanned aerial system, was conducting several flights near the NWC. The SMARTSonde provides measurements of temperature, humidity, pressure, wind speed and direction, and trace gas concentrations. While utilizing a pre-configured flight plan with constant pitch and airspeed, the SMARTSonde was able to retrieve vertical velocities for comparison with the sodar.

3. Observations and Analysis

By analyzing individual pressure traces and trends in the wind field at Mesonet sites across Oklahoma, the gravity wave was tracked across the state. The observed maximum pressure change and time of passing at each location is visualized in Fig. 1. While the gravity wave is fairly weak, with a maximum pressure jump of only 1.2 mb at Wynona, OK, it still had a significant impact on the local weather conditions. An area of cloudiness developed in southwest Oklahoma in association with the gravity wave and progressed to the northeast in conjunction with the movement of the gravity wave.

There was a wind shift associated with the pressure jump as the gravity wave passed. The winds became more southerly as the pressure increased. Whereas the pressure jump recorded at the NWC occurred within only 7 minutes, it took about an hour for the winds to shift from the northeast to the

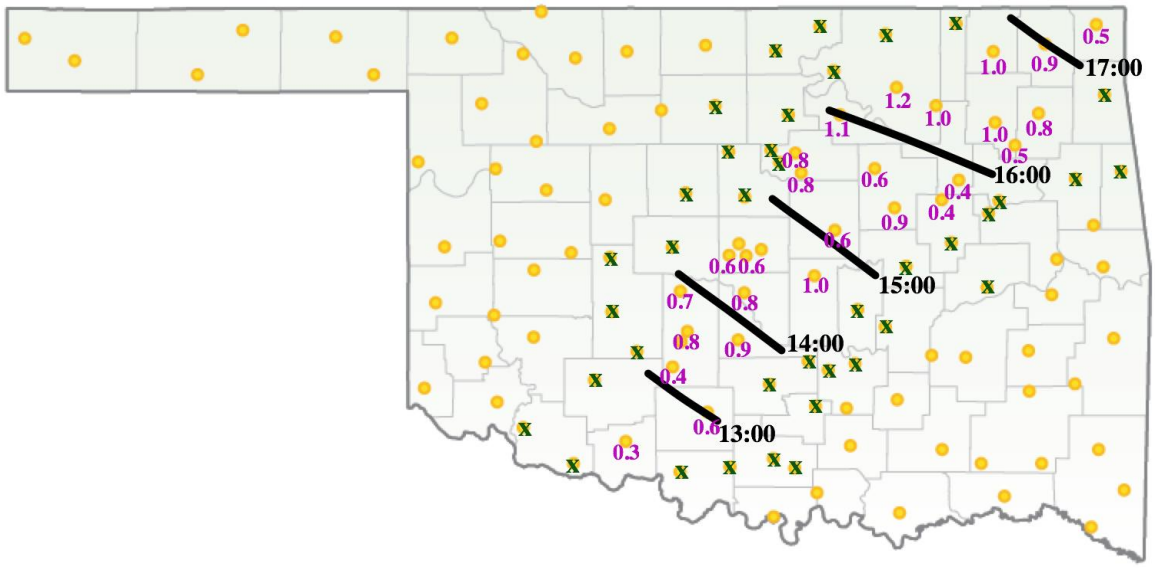

Figure 1. Map of Oklahoma showing the location of the gravity wave at each hour in local time (heavy black line). Dots represent location of Oklahoma Mesonet sites. 'x' indicates no pressure oscillation was observed at the site. Numbers represent the maximum pressure change associated with the gravity wave.

east-southeast. This wind shift agrees with the conceptual model provided by Bosart and Sanders (1986). Sodar retrieved winds show that this wind shift could be observed up to at least 280 m AGL.

Vertical motions retrieved by the sodar indicate that there was mostly rising motion associated with the pressure jump as the crest of the gravity wave approached, which agrees with previous conceptual models. However, between 13:20-13:40 local time (LT), there was significant sinking motion throughout the boundary layer. This agrees with observations from a SMARTSonde flight during the same time period, where sinking motions of up to 1.8 m s^{-1} at only 150 m AGL were retrieved. These negative vertical velocities do not agree with previous conceptual models of gravity waves.

4. Conclusions

Various instruments were used to analyze a relatively weak gravity wave that propagated across Oklahoma on April 26, 2011. In many ways, the observed features of the wave are in agreement with theory. However, there was strong sinking motion just above the surface that coincided with a sharp pressure rise, whereas rising motion would be expected for an ideal gravity wave in theory. There may have been wave interactions or other meteorological phenomena that resulted in the significant sinking motion near the surface at the time.

References

Bosart, L.F. and F. Sanders, 1986: Mesoscale structure in the Megalopolitan Snowstorm of 11-12 February 1983. part iii: A large-amplitude gravity wave. *J. Atmos. Sci.*, **43**, 924-939.

Pothecary, I., 1954: Short-period variations in surface pressure and wind. *Quart. J. R. Met. Soc.*, **80**, 395-401.

McPherson, R.A., C.A. Fiebrich, K.C. Crawford, J.R. Kilby, D.L. Grimsley, J.E. Martinez, J.B. Basara, B.G. Illston, D.A. Morris, K.A. Kloesel, A.D. Melvin, H. Shrivastava, J.M. Wolfinbarger, J.P. Bostic, D.B. Demko, R.L. Elliott, S.J. Stadler, J. Carlson, and A.J. Sutherland, 2007: Statewide monitoring of the mesoscale environment: A technical update on the Oklahoma Mesonet. *J. Atmos. Oceanic Technol.*, **24**, 301-321.

First results of thunderstorm forecast verification in terminal aerodrome forecasts in Croatia

Jadran Jurković*, and Igor Kos*

**Croatia control Ltd, MET Division, Zagreb, Croatia*

1. Introduction

As part of a quality management system, ICAO Annex 3 recommends quality assessment of forecasts. Among the proposed performance measures such as timeliness, coding and formatting of products, forecast verification is one of the most challenging. For aviation purposes, e.g. flight planning, one of the most important forecasts is the Terminal Aerodrome Forecast (TAF).

A thunderstorm (TS) is a typical mesoscale phenomenon. The month with the maximum frequency of days with TSs at Croatian airports has 12-25% such days. The continental part has a typical maximum of convective activity in spring and summer (Mikuš et al. 2012), while the occurrence at the coast is more uniform throughout the whole year with slightly decreased activity towards the south (e.g. Penzar et al. 2001). In aviation forecast and observed weather reports thunderstorms are coded as TS together with possible corresponding precipitation, other related phenomena and cumulonimbus cloud. The impact of thunderstorms and related phenomena on aviation can be hazardous; therefore accurate forecasts are highly desirable.

2. Approach

The verification method initiated in Croatia Control Ltd. is similar to Austrocontrol's verification system described in Mahringer (2008). It is based on verifying the conditions between forecasts and observations for each hour. In the forecast, the hour with TS is considered if mentioned within any group of change (transitions ('from' or 'becoming'), temporary or with probability). Reference observed weather is obtained from the routine METAR report which is released half-hourly. Present weather, recent data (within the past half hour) and data in the vicinity were handled to get the hours with observed TS.

A contingency table for all forecasted hours is computed and consists of an unqualified state that a single TS occurred.

3. Description of experiments

The first results of the verification of TS forecasts for 6 airports are presented. Two airports are situated inland (Zagreb LDZA, Osijek LDOS) and the others are onshore (Pula LDPL, Zadar LDZD, Split LDSP and Dubrovnik LDDU). The data used are TAF and METAR reports in the period 2009-2011. Forecasts are regularly released every 3 or 6 hours with a duration of 9 or 24h for LDOS, LDZD or LDZA, LDPL, LDSP, LDDU, respectively. Overall there are about 500,000 forecasted hours presented in contingency tables for each airport. Typical verification measures (e.g. Wilks 2006) could be assessed from the obtained data.

4. Results

Two attributes of forecast quality, accuracy and bias, are presented. As a measure of accuracy, the proportion correct (PC) is a fraction of the n forecast occasions for which the forecast correctly anticipated a TS event or non-TS event. Bias is the ratio of the number of forecasted TS hours to the number of observed TS hours. The probability of TS (in terms of hours) is 1-1.5 % and therefore, is a

very rare event. PC results (Figure 1a) are better for airports inland and also LDPL which is situated at the top of the Istrian peninsula which is very well known for TS activity (e.g. Mikuš at al. 2012). Contrary to the others, these airports have a significant daily maximum of TS occurrence during the afternoon, which allows a shortened period with TS forecast. This is confirmed in results of bias (Figure 1b) where it is smaller for these airports and greater for the others. Overall, PC and bias results could be improved by shortening the period of TS forecast.

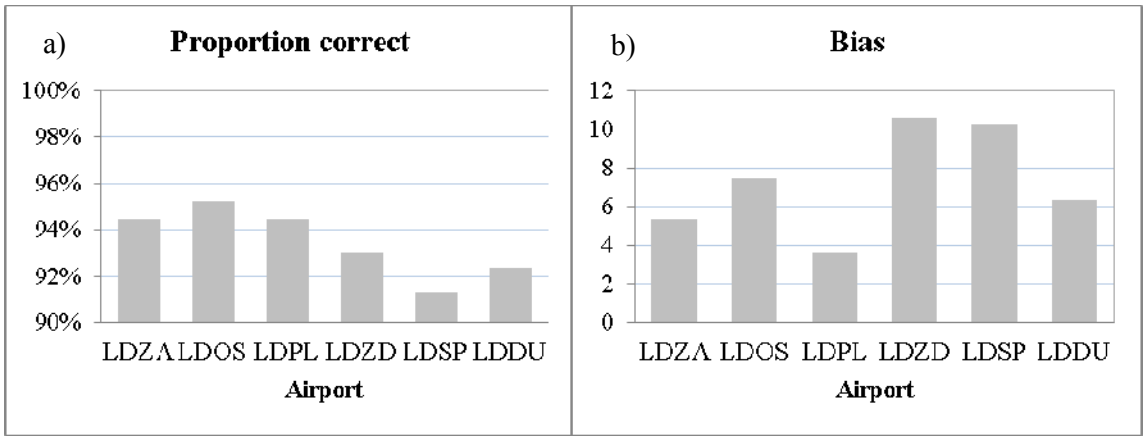

Figure 1. Verification measures: proportion correct (a) and bias (b) for thunderstorms at Croatian airports for the period 2009-2011.

Although it seems that TS forecasts are worse at southern airports, formally they are considered correct. This is due to the definition of forecast temporary period (TEMPO) according to which one outcome during the forecast period is sufficient. Further examination of only the TS forecast period with new contingency tables should be performed. Such results would be more understandable for the forecaster and better related to the intrinsic mesoscale nature of TS which is difficult to forecast for a single point (such as an airport).

5. Conclusions

TAF verification for Croatian airports has recently been initiated. Verification measures, PC and bias, are presented for the TS event. Results are inherent to similar other rare events. Better scores are obtained when the forecast period of TS event is shorter. This is limited by an increased risk of missed TS forecast hours. At continental airports TS forecasts have less bias due to a more pronounced daily maximum of TS which facilitates forecasting and allows the TS forecast period to be shortened.

More useful results for forecasting would be gained with detailed insight into every miss and false alarm event, by relating it to synoptic situations and investigating the lead time and duration of defined forecast TS events.

References

Penzar, B., Penzar, I., and Orlić, M., 2001: *Weather and climate of East Adriatic* (in Croatian). Nakladna kuća Dr.Feletar, Zagreb, 258 pp.

Mahringer, G. 2008: Terminal aerodrome forecast verification in Austro Control using time windows and ranges of forecast conditions. *Meteorol. Appl.*, **15**, 113–123.

Mikuš, P., Prtenjak, M.T., and N. Strelec-Mahović, 2012: Analysis of the convective activity and its synoptic background over Croatia, *Atmos. Res.*, **104-105**, 139.

Wilks, D. S., 2006: *Statistical methods in the atmospheric sciences*. 2nd edn. Academic Press, San Diego, 627 pp.

Mesoscale Features of the 31 January 2011 Oklahoma Storm

Jennifer F. Newman*

**School of Meteorology, University of Oklahoma, Norman, OK*

1. Introduction

The end of January 2011 brought an intense, record-breaking winter storm to Oklahoma. From 31 January to 1 February 2011, bands of thunder-sleet, freezing rain, and heavy snow moved through Oklahoma, resulting in snow accumulations up to 1 foot and wind gusts in excess of 40 mph. Although the main storm system was associated with synoptic-scale forcing, several features suggest that mesoscale processes also influenced the type and distribution of precipitation in Oklahoma.

Several surface observation stations in Oklahoma reported lightning and hail during the evening of 31 January 2011; however, model soundings indicate that the atmosphere was quite stable overnight. The convection may have been associated with Conditional Symmetric Instability (CSI), which, in the past, has been suggested as a possible mechanism for precipitation modulation and convective elements in winter storms (e.g., Wolfsberg et al. 1986). Another mesoscale feature of the event was a series of snow bands, spaced ≈100 km apart. These mesoscale snow bands may have formed in association with ducted gravity waves (e.g., Lindzen and Tung 1976).

In this presentation, CSI and ducted gravity waves are evaluated as potential mechanisms responsible for the mesoscale features of the 31 January 2011 snow storm. These phenomena are examined using soundings, surface observations, and radar and satellite observations.

2. Background

As originally described by Emanuel (1983), CSI theory primarily involves two quantities: the pseudo-angular momentum, m, and the potential temperature, θ, where $m = u - fy$, f is the Coriolis parameter, and u is the component of wind in the zonal direction. It is assumed that these fields are symmetric in the x-direction. In a symmetric atmosphere, the y and z equations of motion of a hypothetical parcel tube can be simplified to the following:

$$\frac{dv}{dt} = -f(m_t - m_g)\,;\, \frac{dw}{dt} = \frac{g}{\theta_o}(\theta_t - \theta_g)$$

where the subscript t refers to the tube and the subscript g refers to the environment. If the parcel is displaced in a slantwise direction such that the angular momentum and/or potential temperature of the environment are different than those of the parcel, the parcel tube will accelerate. A simple method for investigating the potential for CSI involves following a line of constant m_g; if the environmental potential temperature decreases with height or increases weakly with height along this m_g surface, CSI is possible.

Banded convection has also been attributed to gravity waves. Gravity waves arise when an interface between two fluids of different densities is perturbed, for example, by the top of a cumulus cloud. Lindzen and Tung (1976) introduced the concept of ducted gravity waves, waves which are trapped in a stable layer and are able to persist for a long period of time (i.e., several hours).
Ducted gravity waves are possible if a stable lower tropospheric layer is located beneath a less stable or unstable layer in such a way that gravity waves can be reflected toward the ground without significant loss of energy.

3. Results

To investigate the possible existence of CSI, soundings were used to create cross-sections of geostrophic absolute momentum, m_g, and equivalent potential temperature, θ_e. A vertical cross-section was taken along a southwest-northeast oriented line extending from Texas to Michigan,

approximately parallel to the thermal wind shear vector. At heights from 2 to 3 km above KOUN (Norman, Oklahoma), θ_e decreased with height along the m_g = –40 m s^{-1} surface at 0000 UTC; this suggests that CSI was possible over central Oklahoma at this time. Since the m_g surfaces were vertically-oriented, a large meridional path would not need to be taken to realize this region of CSI.

Pressure and wind fluctuations associated with the gravity wave were observed by the Oklahoma Mesonet, a series of weather observation stations across the state of Oklahoma. Several mesonet stations showed a drop in sea-level pressure and a shift in wind direction as the trough of the gravity wave passed through; an example from one of these stations is shown in Fig. 1. The phase speed of the gravity wave was estimated from the Mesonet observations; a value of 28.9 m s^{-1} was obtained, which agreed well with the theoretical ducted gravity wave speed.

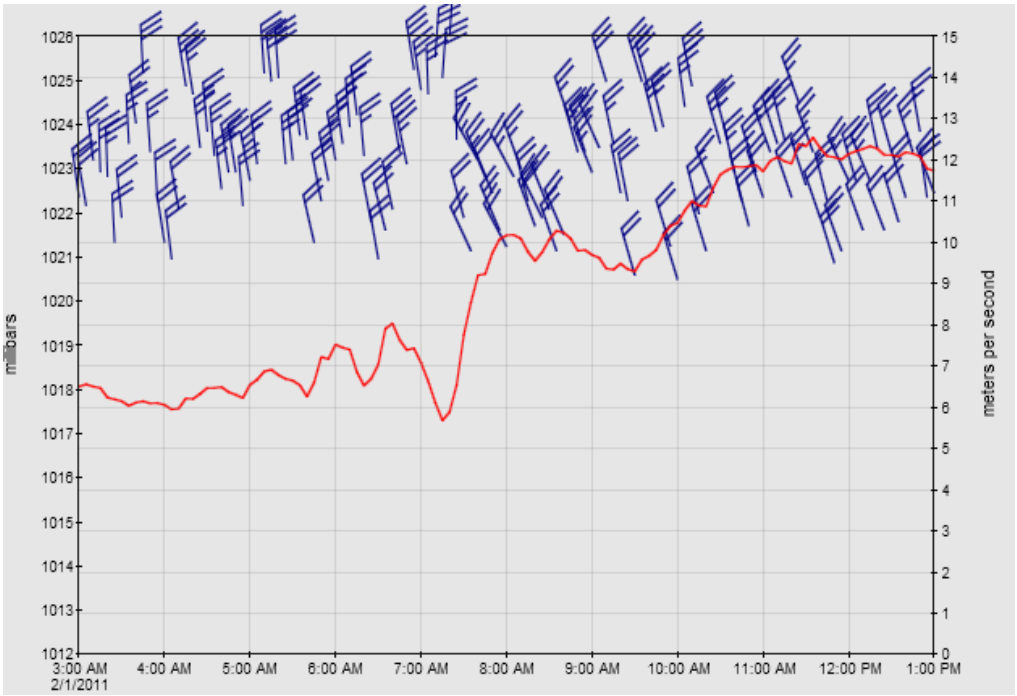

Fig. 1. Sea-level pressure (solid line, in mb) and wind speed and direction (barbs, in m s^{-1}) time series on 1 February 2011 from Mesonet station in Ninnekah, Oklahoma. Gravity wave troughs occurred at approximately 7:15 and 9:30 am.

5. Summary and Conclusions

Based on the presence of convective elements and precipitation modulation, it appeared likely that mesoscale processes occurred during the Oklahoma winter storm of 31 January 2011. Vertical profiles of m_g and θ_e indicated that CSI was possible over central Oklahoma during the late evening hours of 31 January 2011. However, there were likely other mesoscale processes occurring at that time (e.g., frontogenesis), so convective elements in the storm cannot be attributed only to CSI. A gravity wave also occurred during the winter storm. Pressure and wind fluctuations associated with the gravity wave were observed in great detail by the Oklahoma Mesonet, and agreed well with conceptual models of ducted gravity waves.

References

Emanuel, K. A., 1983: On assessing local conditional symmetric instability from atmospheric soundings. *Mon. Wea. Rev.*, **111**, 2016–2033.

Lindzen, R. S. and K.-K. Tung, 1976: Banded convective activity and ducted gravity waves. *Mon. Wea. Rev.*, **104**, 1602–1617.

Wolfsberg, D. G., K. A. Emanuel, and R. E. Passarelli, 1986: Band formation in a New England winter storm. *Mon. Wea. Rev.*, **114**, 1552–1569.

POSTER

PRESENTATIONS

Atmospheric conditions associated with the windstorm "Vento Norte" in southern Brazil: a preliminary analysis

Ernani L. Nascimento*, and Marcos L. Chamis*

**Department of Physics, Universidade Federal de Santa Maria, Santa Maria/RS, Brazil.*

1. Introduction

During the austral cold season a windstorm named "Vento Norte" (VN; Portuguese for North Wind) is occasionally observed in central Rio Grande do Sul (RS) — the southernmost state in Brazil. A typical VN episode comprises fairly strong northerly winds lasting for several hours, accompanied by a substantial rise in both surface air temperature and dew point depression. These characteristics appear to be more evident just at and downstream of a modest (less than 400m high) leeward slope that is perpendicular to the prevailing wind direction. This observation suggests a possible role played by the topography in the behavior of the winds, as in Decker and Robinson (2011).

This article aims at: (a) summarizing a first attempt to objectively identify events of VN based on surface observations; (b) describing the atmospheric conditions associated with the VN.

2. Data and methodology

Hourly surface meteorological observations from April 2002 to August 2009 obtained from Brazil National Meteorological Institute´s automated weather station (INMET-AWS) located in Santa Maria/RS (29°43.5´S;53°43´W) — 4.5km downstream of the zonally-oriented leeward slope — is used to objectively detect episodes of VN. The proposed criteria to identify VN events are: (i) wind gusts ranging within 300° (WNW) and 30° (NNE) must be sustained at or above 40km/h (~11m/s) for at least 4 consecutive hours; (ii) during this same period, the hourly surface air temperature must be observed at or above its corresponding 90th percentile [75th percentile] during more than 50% of the event [during the entire event]. (Only data from the austral cold season — April to October — was inspected). For the selected dates, bi-daily (00Z and 12Z) upper-air observations conducted at Santa Maria Air Force Base (SBSM) were examined, as well as meteorological fields obtained from the 0.5° grid-spacing NCEP Climate Forecast System Reanalysis (CFSR; Saha et al. 2010).

3. Results

A total of 66 VN episodes were detected with the criteria mentioned above. An ongoing subjective

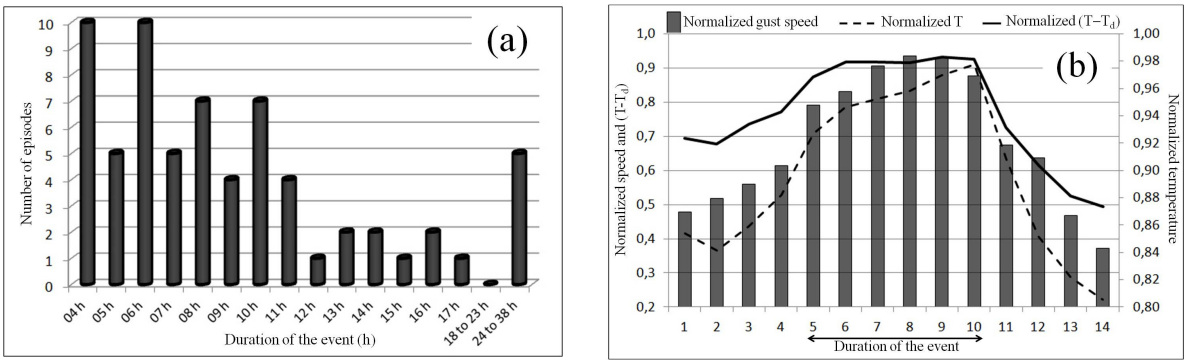

Figure 1. (a) Number of VN episodes as a function of their duration; (b) Average hourly evolution of gust speed, temperature and dew point depression — normalized by their corresponding maximum values — for ten 6hr-long VN events. In the abscissa, 1-4 [11-14] indicate the 4 hours prior to [after] the event, and 5-10 the 6-hr period of the event.

case-to-case analysis is necessary to verify whether some of the shorter events are, actually, part of single longer events. The preliminary distribution of the 66 events as a function of their duration is shown in Figure 1a. Most objectively-identified VN events lasted from 4h to 10h, but 5 episodes lasted for more than 24h. Figure 1b depicts the average hourly variation of (normalized) gust speed, temperature and dew point depression for the ten 6-hr long events. As expected, a rise [drop] in temperature and dew point depression accompanies the strengthening [weakening] of the wind gusts.

The majority (71%) of the 66 events initiated in between midnight and 10AM LST, while around 60% of them dissipated between 11AM and 5PM LST. The most frequent initiation [dissipation] time was in between 1AM-2AM [3PM-4PM]. The preferential nocturnal/early morning initiation combined with the prevailing late morning/afternoon dissipation suggest an influence of the stability conditions on such wind system, to be further evaluated.

Figure 2 summarizes the synoptic conditions observed half-way during the 16 August 2009 episode which lasted for 17 hours with surface wind gusts peaking at 22 m s^{-1}. Surface cyclogenesis (Fig. 2a) was under way over the far east La Plata Basin driving northerly and northwesterly winds over RS (Fig. 2b), which is a common synoptic pattern preceding VN events. Surface temperatures rose significantly above average for that time of the day (9AM LST) (Fig. 2a). The SBSM sounding shows an inversion close to the surface (Fig. 2c) in a dry boundary layer. This is followed by an (sort of) elevated mixed layer above 850hPa. Aloft, significant midtropospheric dryness is observed, which suggests the presence of subsidence at that level. Some of these characteristics are common to environments conducive to downslope windstorms (e.g., Decker and Robinson, 2011).

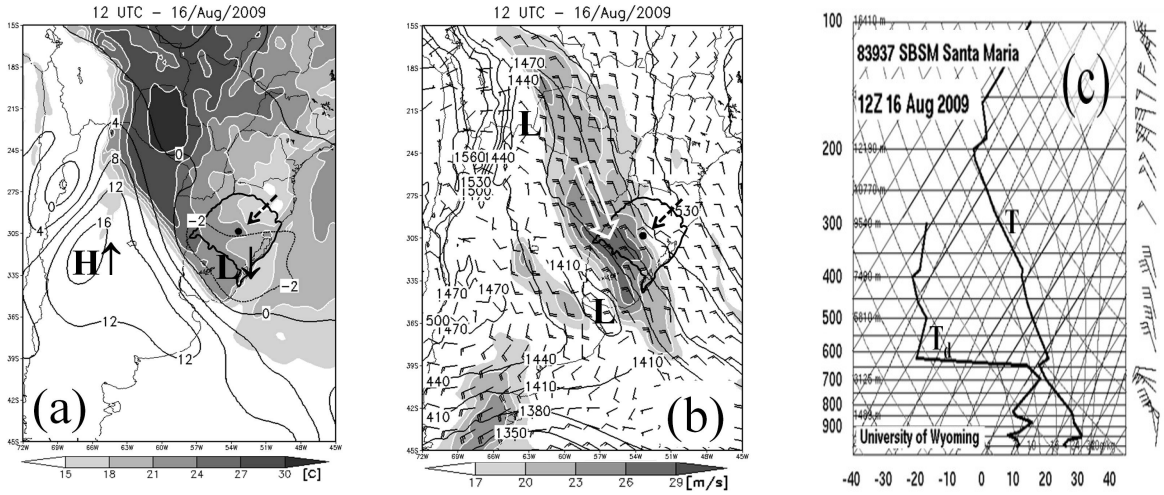

Figure 2. Data valid at 12Z, 16 Aug 2009: (a) air-temperature at 2m (shaded;°C) and 24-hr change in sea level pressure (contours; hPa) from NCEP-CFSR; (b) 850hPa heights (contours; gpm) and winds (barbs and shading; m/s) from NCEP-CFSR; (c) skew-T diagram for the SBSM sounding.

5. Conclusion

The method (algorithm) employed to objectively identify the occurrence of VN episodes based on surface observations managed to detect several true VN events, but a subjective fine tuning is still needed in order to better characterize the initiation and dissipation times (and, thus, duration) of the VN. Moreover, such fine tuning is necessary in order to highlight the events that are more clearly forced by mesoscale processes (namely, orography) rather than just by the large scale forcing.

References

Decker, S. G., and D. A. Robinson, 2011: Unexpected high winds in northern New Jersey: a downslope windstorm in modest topography. *Wea. Forecasting*, **26**, 902-921.

Saha, S., and collaborators, 2010: The NCEP Climate Forecast System Reanalysis. *Bull. Amer. Meteor. Soc.*, **91**, 1015-1057.

Use of rapid scan satellite imagery and ground sensors to identify and plot the evolution of a convective heat burst

Jay Trobec

KELO-TV, Sioux Falls, South Dakota, USA

1. Introduction

A heat burst (Johnson, 1983) is defined as a "localized, sudden increase in surface temperature associated with a thunderstorm, shower, or mesoscale convective system" (Glickman, 2000). A heat burst which occurred in Sioux Falls, South Dakota early in the morning of 11 August 2007 took place in close proximity to both the KFSD WSR-88D radar, and to privately-owned mesonet sensors which record data in one-minute increments. During this event, the GOES-12 satellite was in rapid scan operation over the area of interest, collecting imagery every 5-10 minutes.

The combined dataset provides a unique look at this event on a temporally fine scale.

2. Background

A typical atmospheric profile for downburst production includes a layer of warm and dry air above the surface, making rain-free downdraft air conducive to strong adiabatic compression and warming as it descends. Strong surface winds are often observed as the descending parcel makes contact with the surface.

This event began with the decay of a convective rainshower, when precipitation a few hundred meters AGL descended to the ground and was immediately followed by the heat burst.

3. Data collection

Two mesonet sensors two km apart reported a marked temperature increase rate averaging 0.22°C (0.4°F) per minute. Barometric pressure fell at an average rate of 0.13 mb per minute during the combination precipitation/heat burst period. The rise and fall of heat burst temperatures concluded within 45 minutes (Fig. 1).

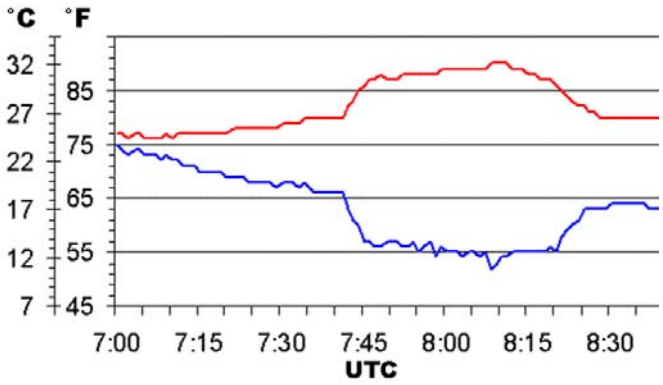

Figure 1. Temperature and dew point trace from the Washington Pavilion sensor in Sioux Falls.

Since a heat burst is a "top-down" atmospheric process, in some cases it may be identifiable by satellite. During this event, a small but intense temperature gradient appeared in the convective cloud top before – and was sustained during – the heat burst (Fig. 2). The temperature minimum in the IR

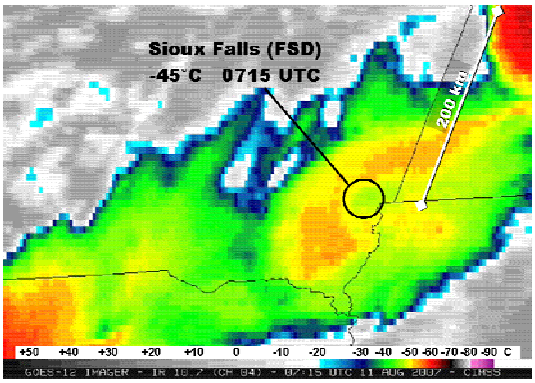

Figure 2. GOES-12 10.7 μm IR image preceding the event, with localized area of warming over Sioux Falls.

imagery was directly above the mesonet sensors. Precipitation was recorded on radar during the onset of the heat burst, but reflectivity returns diminished rapidly (Fig. 3).

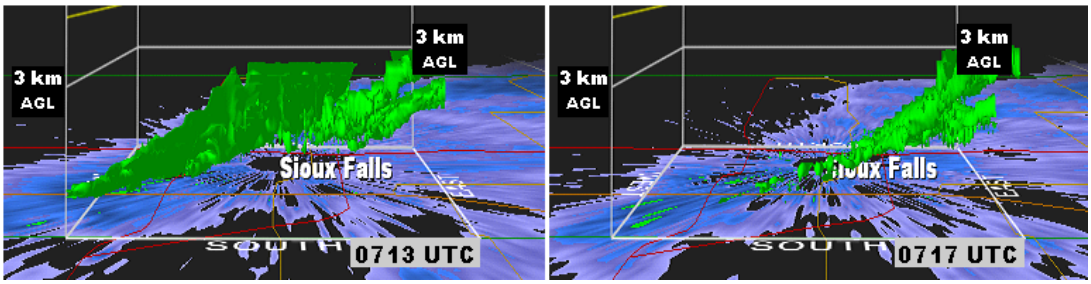

Figure 3. Vertical slice from KFSD radar. Green color represents reflectivity ≥35 dBZ. Box dimensions 12 km x 12 km.

4. Results

Since the mechanics of a heat burst are similar to a downburst, the satellite signatures appear similar. The sequence of IR images shows a localized collapse of the cloud top preceding detection of the heat burst. This collapse is seen as a region of warming, in which the canopy warmed from -55°C to -45°C in the 30 minutes before the heat burst. This collapse is simultaneously reflected in a sharp decrease in atmospheric pressure at the surface. The steepest surface temperature rise/dew point fall occurred 20 minutes later.

The one-minute data shows that a heat burst is not strictly a linear event; rather after the initial increase, the temperature rises and falls undulate during the heat burst. The heat burst is preceded by a sharp decrease in barometric pressure, though the pressure trace also fluctuates during the event. The results were similar in all five mesonet sensors located within 60 km of Sioux Falls.

The fluctuating nature of the surface variables during a heat burst would be consistent with what one might expect in conceptualizing air radiating away from the center of a downburst, although additional studies of more events would be required before a final conclusion.

5. Conclusion

The time sequence showing the cloud top collapse in I-R imagery suggests there may be some predictability of heat bursts, though it might be difficult with satellite analysis alone to distinguish between a heat burst and an ordinary downburst. (Knowledge of the atmospheric profile might aid in discernment.) In either case, an operational meteorologist might gain advance expectation of resulting strong or damaging winds at the surface.

References

Glickman, T., ed., 2000: *Glossary of Meteorology*, 2nd edition. Amer. Meteor. Soc., Boston.

Johnson, B.C., 1983: The heat burst of 29 May 1976. *Mon. Wea. Rev.*, **111**, 1776–1792.

Extrapolated radar reflectivity assimilation into an NWP model

Petr Zacharov*, Zbyněk Sokol

**Institute of Atmospheric Physics ASCR, Prague, Czech Republic*

1. Introduction

Numerical very short-range precipitation forecasts fundamentally depend on the initial model conditions. Relationships among model variable values in the initial conditions are important to forecasting because they determine the future development of model variables and, specifically, the development of precipitation. Various data assimilation techniques have been developed to prepare the initial model conditions. Those integrate a numerical weather prediction (NWP) model over an interval of time (an assimilation window), during which observed data are assimilated into the model. The aim of the assimilation is that the model state at the end of the assimilation window represents the optimum initial conditions for the following model integration.

2. Model description

The forecasts were performed with version 4.11 of the COSMO NWP model, which is a non-hydrostatic and fully compressible model formulated in advection form. The model equations are formulated in finite differences with a terrain-following grid and in rotated spherical coordinates (Baldauf *et al.*, 2011). The model was integrated over the area covering the Czech Republic (central Europe), which comprises 281 by 211 grid points with a horizontal resolution of 2.8 km and 50 vertical levels. The time step was 30 s. The model is able to resolve and explicitly simulate at least the larger-scale elements of organised convection. Therefore, the parametrization of deep convection was not used. The parametrization of shallow convection was included. The model utilised Lin–Farley–Orville type standard one-moment microphysics and considered five classes of hydrometeors (rain water, cloud water, snow, ice and graupel). The initial and lateral boundary conditions are interpolated from the prognostic fields of the COSMO-EU model, which is operated by the German Weather Service, and its horizontal resolution is approximately 7 km.

3. Verification

The forecasts were verified against the precipitation obtained by combining radar-derived precipitation and hourly gauge data. To evaluate the forecasts, we employed two verification methods. We applied Fractions Skill Score (FSS: Roberts and Lean, 2008) and SAL (Wernli *et al.*, 2008), which are both skill scores. The FSS compares the fractional coverage in forecasts with the fractional coverage derived from observations over different-sized neighbourhoods (squares). The fractional coverage is determined as the number of points that have values exceeding a given threshold. Therefore, the FSS depends on the size of the squares and on the threshold values that are used to calculate the fractional coverage. FSS values range from 0 (completely wrong forecast) to 1 (perfect forecast). The SAL evaluates precipitation forecasts simultaneously from several viewpoints. SAL is an object-based quality measure, which contains three distinct components that consider aspects of the structure (S), amplitude (A), and location (L) of the precipitation field. The objects are defined as continuous areas of grid points with precipitation values greater than or equal to a given threshold. From the values of the components S, A and L it can be deducedwhether the model overestimates or underestimates precipitation, whether the shape of precipitation is similar to the observations or too sharp or too spread out.

4. Conclusions

The assimilation of extrapolated radar reflectivity improves precipitation forecasts for the 1st, 2nd and 3rd lead hours as compared to the assimilation of observed data in the majority of cases. The improvement was confirmed for all three hours by all applied evaluation techniques, including a subjective visual evaluation and the objective measures.

The accuracy of the precipitation forecasts depends on the accuracy of extrapolated radar reflectivity. A significantly incorrect extrapolation may lead to a worse precipitation forecast than is obtained using the standard assimilation of observed values. We identified one such case in our forecast set. In this case, observed rain rates were increasing over time and reached an apparent maximum just at the end of the assimilation window before starting to decrease. The maximum rain rate was extrapolated and assimilated into the model, and caused an overestimation of the forecasted precipitation. The described temporal development of observed rain rates, however, is difficult to forecast, and the standard assimilation of observed data also apparently overestimated precipitation.

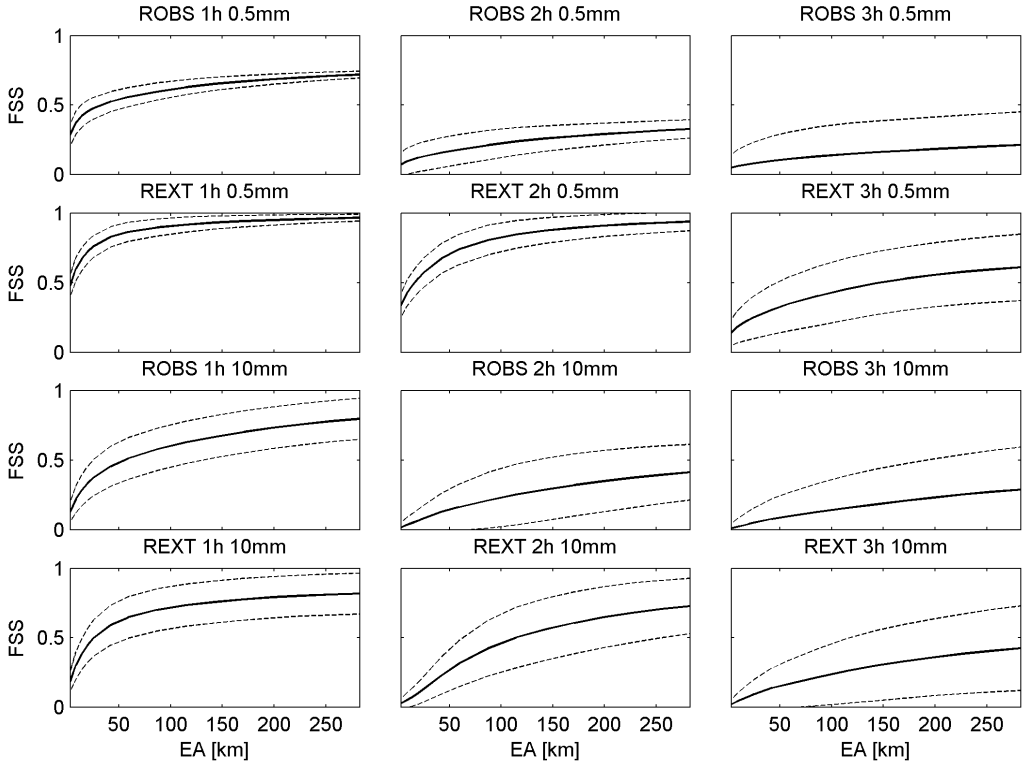

Figure 1. The evaluation of the forecasts by Fractions Skill Score. The horizontal axis shows the sizes of the squares for which FSS (vertical axis) is calculated. The titles indicate forecast hours, thresholds and the assimilation method used. Full lines depict mean FSS over all forecasts and dashed lines show the mean ± standard deviation of FSS over all forecasts.

4. Acknowledgements

This work was supported by grants GACR 205/07/0905 and GACR P209/12/P701 The COSMO code, provided by the German Weather Service,was highly appreciated. The radar and gauge data used in this work was made available by the Czech Hydrometeorological Institute.

References

Baldauf, M,, Seifert, A., Förstner, J., Majewski, D., Raschendorfer, M., Reinhardt, T., 2011: Operational convective-scale numerical weather prediction with the COSMO model: Description and sensitivities. *Mon. Weather Rev.,* **139,** 3887-3905.

Roberts, N.M., Lean, H.W., 2008: Scale-selective verification of rainfall accumulations from high-resolution forecasts of convective events. *Mon. Weather Rev.* **136**: 78–97.

Wernli, H., Paulat, M., Hagen, M., Frei, C., 2008: SAL – A novel quality measure for the verification of quantitative precipitation forecasts. *Mon. Weather Rev.* **136**: 4470–4487.

Revealing Errors in Model Microphysics Parameterizations with Polarimetric Radar and Explicit Modeling

Matthew R. Kumjian*

** Cooperative Institute for Mesoscale Meteorological Studies, University of Oklahoma, Norman, Oklahoma, USA*

1. Introduction and Background

Currently, there are two approaches used to account for cloud and precipitation physics in storm-resolving numerical weather models: bulk parameterizations, where a functional form of the particle size distribution (PSD) is assumed, and "bin" or spectral methods, in which the number of particles in each size "bin" is allowed to vary independently via different kinematic and microphysical processes. Polarimetric radar measurements are very sensitive to changes in shape of the PSD, especially those occurring for the largest sizes. The polarimetric radar variables are reflectivity factor at horizontal polarization Z_H, differential reflectivity Z_{DR}, specific differential phase K_{DP}, and the co-polar correlation coefficient ρ_{hv} (for a review, see Zrnić and Ryzhkov 1999). By converting the model microphysical output into these polarimetric radar variables, one can make direct comparisons between the types of signatures observed in real storms and those simulated with numerical models (e.g., Jung et al. 2010; Ryzhkov et al. 2011; Kumjian and Ryzhkov 2012). Errors resulting from assuming PSD shapes *a priori* (as is done in parameterizations) can significantly affect simulated fields of polarimetric radar variables, thereby causing problems for assimilation of polarimetric observations into numerical models.

2. Experimental Approach

Here, we quantify errors in the simulated polarimetric radar variables resulting from assumptions about the PSD used in bulk parameterization schemes. The benchmark for such comparisons are explicit "bin" microphysics models, including simple one- and two-dimensional models describing sedimentation (Kumjian and Ryzhkov 2012; herein KR12), evaporation of raindrops (KR10), stochastic freezing of drops within updrafts (Kumjian et al. 2012), and size sorting by wind shear (KR12). The microphysical model output is converted to the radar variables by employing the operator described in Ryzhkov et al. (2011). Results are compared to experimental polarimetric radar observations.

3. Discussion of Results and Conclusions

Results of these comparisons illustrate that substantial errors are possible in bulk parameterizations, owing to incorrect treatment of microphysical processes and inappropriate assumptions regarding PSD shape. This is especially true for processes that preferentially affect a certain part of the PSD. For example, size sorting preferentially acts to decrease the concentration of smaller particles, resulting in a narrowing of the PSD. Single-moment (1M) bulk schemes and double-moment (2M) schemes with a fixed spectral shape parameter are incapable of narrowing the PSD, resulting in large errors in excess of 2 dB in magnitude (Fig. 1). Three-moment (3M) schemes (e.g., Milbrandt and Yau 2005) are capable of narrowing the PSD, thereby producing more realistic fields of the radar variables for processes such as sedimentation and size sorting (Fig. 1c). However, excessive narrowing beyond what is observed in nature can also lead to errors, as the narrowing erroneously removes larger particles from and adds medium-sized particles to the PSD, as summarized in the schematic Fig. 2. Relative 3M errors in Z_{DR} and K_{DP} can be as large as 20%. Because of this, it is recommended that a limit be imposed on the shape parameter, which controls narrowing. Based on results of KR12, we recommend a maximum shape parameter of 20 – 30.

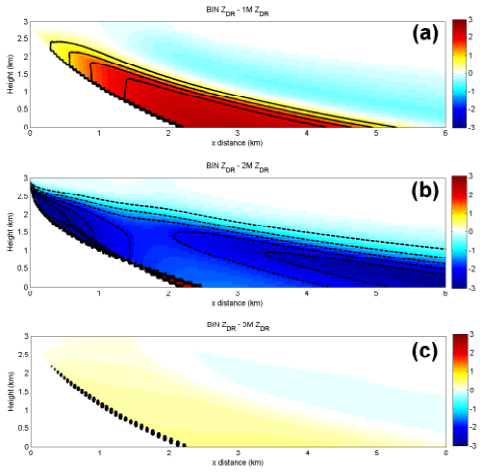

Figure 1. Difference in fields of Z_{DR} between the wind shear model bin solution and (a) 1M, (b) 2M, and (c) 3M bulk parameterizations. Contours in 0.5-dB increments are overlaid (solid for positive differences, dashed for negative differences). From KR12.

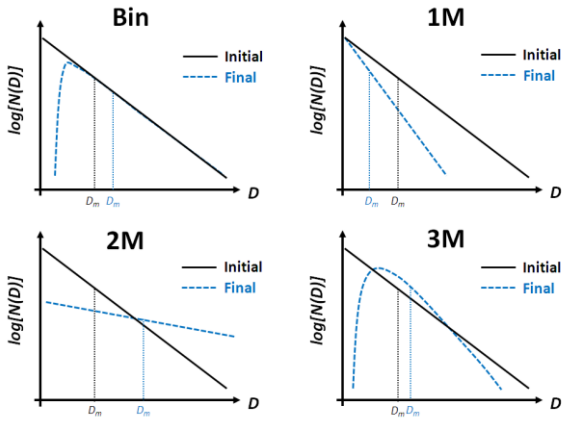

Figure 2. Schematic illustrating the sources of error in modeling the PSD with parameterization schemes for a microphysical process that preferentially depletes smaller particle sizes (e.g., size sorting, evaporation, melting).

Aside from using a computationally expensive third prognostic moment, several methods have been proposed to address these concerns, including the use of a *diagnostic* third moment (e.g., Milbrandt and Yau 2005). Care must be taken when considering these methods, especially when used in conjunction with polarimetric radar data (e.g., data assimilation). Though changes to the PSD tail do not significantly affect model variables such as total particle mass or number concentration, they dramatically affect the radar variables. Thus, small errors in the PSD can contribute to large errors in the simulated radar variables.

References

Jung, Y., M. Xue, and G. Zhang, 2010: Simulations of polarimetric radar signatures of a supercell storm using a two-moment bulk microphysics scheme. *J. Appl. Meteor. Clim.*, **49**, 146-163.

Kumjian, M.R., and A.V. Ryzhkov, 2010: The impact of evaporation on polarimetric characteristics of rain: Theoretical model and practical implications. *J. Appl. Meteor. Clim.*, **49**, 1247-1267.

Kumjian, M.R., and A.V. Ryzhkov, 2012: The impact of size sorting on the polarimetric radar variables. *J. Atmos. Sci.*, **in press**.

Kumjian, M.R., S.M. Ganson, and A.V. Ryzhkov, 2012: Freezing of raindrops in deep convective updrafts: A microphysical and polarimetric model. *J. Atmos. Sci.*, **in review.**

Milbrandt, J.A., and M.K. Yau, 2005: A multimoment bulk microphysics parameterization. Part II: A proposed three-moment closure scheme and description. *J. Atmos. Sci.*, **62**, 3065-3081.

Ryzhkov, A.V., M. Pinsky, A. Pokrovsky, and A. Khain, 2011: Polarimetric radar observation operator for a cloud model with spectral microphysics. *J. Appl. Meteor. Clim.*, **50**, 873-894.

Idealized simulations of wave-induced boundary-layer separation in the lee of mesoscale topography

Stefano Serafin*, Lukas Strauss* and Vanda Grubišic*,**

*Department of Meteorology and Geophysics, University of Vienna, Vienna, Austria
**Earth Observing Laboratory, National Center for Atmospheric Research, Boulder, CO, USA

1. Introduction

A boundary layer is a region of fluid flow affected by friction against an external body. Although boundary layers form at such an interface, they may separate from it under the action of an adverse pressure gradient force. The event of boundary-layer separation (BLS) is known to occur even in the atmosphere and has often been associated to several phenomena typical of the lee side of mountains. These include for instance terrain-induced rotors and banner clouds. Laboratory experiments (Baines 1995) and theoretical studies (Marshall and Ambaum 2005) of 2D stratified flow over a hill reveal a range of separation regimes dependent on the parameters Nh/U (non-dimensional obstacle height) and h/L (aspect ratio or slope steepness), where N and U are the buoyancy frequency and upstream wind speed, and h and L the mountain height and half-width. During non-linear flow over obstacles of moderate steepness ($Nh/U \gg 1$, $h/L \ll 1$), pressure perturbations generated by gravity waves outside the boundary layer become important and make wave-induced BLS possible.

BLS in stratified flows has been observed and described in laboratory experiments, while its possible occurrence in the atmosphere has been investigated mostly in conjunction with the study of trapped lee waves and atmospheric rotors (Doyle and Durran 2002). However, it has only recently been observationally documented, by means of airborne cloud radar over the lee of the Medicine Bow range in Wyoming (Haimov et al 2008). An important feature of the Medicine Bow observations is the non-steadiness of the wave-BLS-rotor system, which appeared to move upstream along the lee slope for about 8 km in the ~35 min lag between two consecutive flight legs.

2. Objectives

So far, laboratory and analytical investigations of BLS in continuously stratified flows have only focused on the dependence of the phenomenon on a limited set of governing parameters (e.g., obstacle aspect ratio and nonlinearity, as mentioned above). Several modeling studies on rotors concentrated on the possible impact of other factors, including for instance the presence of inversion layers in the upstream flow. However, a focus on the possible non-stationary behavior of rotor circulations was generally missing. An analysis of the mechanisms leading to non-stationary trapped lee waves (which, in combination with surface friction, may lead to BLS and rotors), was carried out by Nance and Durran (1998). Based on 2D simulations of flow over a frictionless obstacle, they suggest that fast variations in lee wave patterns can be traced back to non-linear wave dynamics.

The objective of our study is to analyze the impact of surface friction on BLS, in order to understand how it may affect the exact location of flow detachment and the onset of non-stationary perturbations. The observed Medicine Bow event is taken as a benchmark case. A series of semi-idealized large-eddy simulations (LES) were made using the CM1 model (Bryan and Fritsch 2002). Simulations have grid increments of 50 × 20 m respectively in the horizontal and vertical directions and use upstream profiles of wind speed and potential temperature derived from the available observations. Simulations consider a simplified 2D geometry where the complex topographic obstacle is represented as a linear mountain ridge with approximately the same size and shape as the Medicine Bow range, but they are fully 3D allowing for realistic turbulence dynamics. Surface friction is parameterized using a drag relationship. Model runs differ in the specification of the drag coefficient, allowing an investigation of the impact of friction on BLS.

3. Results

The simulated flow field bears strong resemblance with the existing observations. Downslope flow with intensity in excess of 30 m s^{-1} detaches from the ground with a strong updraft. Downstream of this, a patch of considerably lower wind intensities is found, with embedded occasional reverse flow. The thin sheet of positive horizontal vorticity at the ground breaks down into several small vortices within the rotor region. The near-surface rotor circulation is associated with a large hydrostatic wave aloft, breaking at an altitude between 2000 and 5000 m a.g.l.

Simulations confirm that a non-stationary behavior of the separation point, as observed over the Medicine Bow range, is possible under some circumstances. Surface friction seems to cause the transition from a regime where the rotor circulation moves steadily downstream to others where the location of the separation point is stationary in time. In the case of extremely high bottom friction, separation tends to occur only slightly downstream of the mountaintop, suggesting that increasing friction may drive the system towards the bluff-body BLS regime observed in neutrally stratified flows. A steady upstream motion of the wave-rotor system was not found in any of the simulations. Fast-moving perturbations potentially linked to wave resonance, as suggested by Nance and Durran (1998), were also not found in simulations.

Although the rotor region evolves on time scales of the order of hours, its interior features a succession of velocity maxima with a much shorter characteristic time scale, of the order of a few minutes. These fluctuations seem to be related to a series of wavelike disturbances that, apparently, develop as Kelvin-Helmholtz billows along a stable layer with intense wind shear, lying upstream of the obstacle at an altitude of ~3500 m a.g.l..

4. Conclusions

Preliminary LES simulations show the sensitivity of the rotor dynamics to increasing surface friction, which enhances flow deceleration on the lee of the obstacle and shifts the separation point upstream. The amplitude of wavelike motions downstream of the ridge also decreases with increasing friction, leading to less intense rotor circulations.

Results also confirm that dynamic instability along a shear line can be responsible for rapid oscillations (pulsations) in the intensity of the near-surface flow, both in the downslope wind region and within the rotor. While the occurrence of pulsations in downslope winds is well known (Belušić et al 2007), and is generally related to the strong shear existing between a stagnant gravity-wave-breaking region and the underlying accelerated downslope wind, the recognition of the possible occurrence of pulsations within a rotor likely represents a novel result.

References

Ambaum, M.H.P. and D.P. Marshall, 2005: The effects of stratification on flow separation. *J. Atmos. Sci.*, **62**, 2618-2625.

Baines, P.G., 1995: Topographic effects in stratified flows. Cambridge University Press, 482 pp.

Belušić, D., M. Žagar and B. Grisogono, 2007: Numerical simulation of pulsations in the bora wind. *Q. J. R. Meteorol. Soc.*, **133**, 1371-1388.

Bryan, G.H., and J.M. Fritsch, 2002: A benchmark simulation for moist nonhydrostatic numerical models. *Mon. Wea. Rev.*, **130**, 2917–2928.

Doyle, J.D., and D.R. Durran, 2002: The dynamics of mountain-wave-induced rotors. *J. Atmos. Sci.*, **59**, 186–201.

Haimov, S., V. Grubišić, J. French, and L. Oolman, 2008: Multi-Doppler measurements of atmospheric rotors and turbulent mountain waves. IEEE IGARSS Symposium, Boston, MA.

Nance, L.B. and D.R. Durran, 1998: A modeling study of nonstationary trapped mountain lee waves. Part II: Nonlinearity. *J. Atmos. Sci.*, **55**, 1429–1445.

Verification of global instability indices, derived from satellite data over wider Croatian area

Ivan Smiljanić*, Nataša Strelec Mahović*, and Maja Telišman Prtenjak**

**Meteorological and Hydrological Service of Croatia, Zagreb, Croatia*
***AMGI, Department of Geophysics, Faculty of Science, University of Zagreb, Zagreb, Croatia*

1. Introduction

A deep, moist convection that occurs in the 'clean air' is one of almost daily occurrences in the atmosphere of our latitudes, and elsewhere. Unlike e.g. the frontal convection, convection in 'clean air' is harder to predict. These are situations when in the morning we have 'quiet' atmosphere, but a few hours after coming to the intensive development of convective clouds, which are among other things, the cause of many material damages. Therefore in this work we used four indices of instability (K, KO, LI and TPW), whose values may very well indicate areas in an atmosphere suitable for the development of severe convection. The aim was to make their verification over greater area of Croatia. Indices were obtained by synthesis of short-term forecasts and satellite measurements, with the help of 'Physical Retrieval Method' (i.e. PRM) method. As such, they have much better spatial and temporal resolution (if compared with radio-sounding measurements), and cover large areas (e.g. greater than the radar measurements). A verification of the indices is made for four summer days and for one day in the winter season.

2. Indices and PRM method

Instability index values are associated with the probability of occurrence of the convective development. In other words, it is possible to determine the typical threshold for each index, above or below which it will represent the stability or instability of the atmosphere. These thresholds are not fixed, but can vary depending on observed season, synoptic conditions, geographical location and climatic conditions of the observed area.

The goal of PRM method is to find the vertical profiles of temperature and humidity, using satellite measurements of radiation of the Earth and its atmosphere, and using these profiles to gain the required indices of instability. For this purpose so-called 'inversion technique' is used to find the vertical profiles of temperature and humidity that best simulate the radiation recorded at the top of the atmosphere (i.e. satellite image) (Rodgers, 1976). There are many combinations of vertical profiles of temperature and moisture that could give the same radiation image. Therefore iterative scheme is applied. It is performed insomuch that first is determined the initial background profile, so-called 'first guess', in our case that would be 6-hour forecasts of a numerical model (ECMWF). Then, from step to step profile is gradually modified to obtain the radiation corresponding to the satellite image. Iterative scheme is usually stopped at that stage in which the brightness temperature difference, in 6 satellite channels, is less than 1.5 K (König and de Coning, 2008).

3. Methods of verification

The first method of verification is a visual comparison of the distribution and intensity of indices, and the development of convective clouds. This is a subjective insight into causal connection between instability indices and the development of convection, but it is not completely reliable way to obtain tangible evidence of correlation between instability and convective processes. For this reason, other methods of verification are used.

Second kind of verification is based on a comparison of morning index values with the development of convective instability later in the day, via the number of detected lightning (Fig. 1). Each of the four indices was averaged in the four morning hours and was compared with next 10-

hour sum of detected lightning. This is more objective way of verification and can give more reliable results.

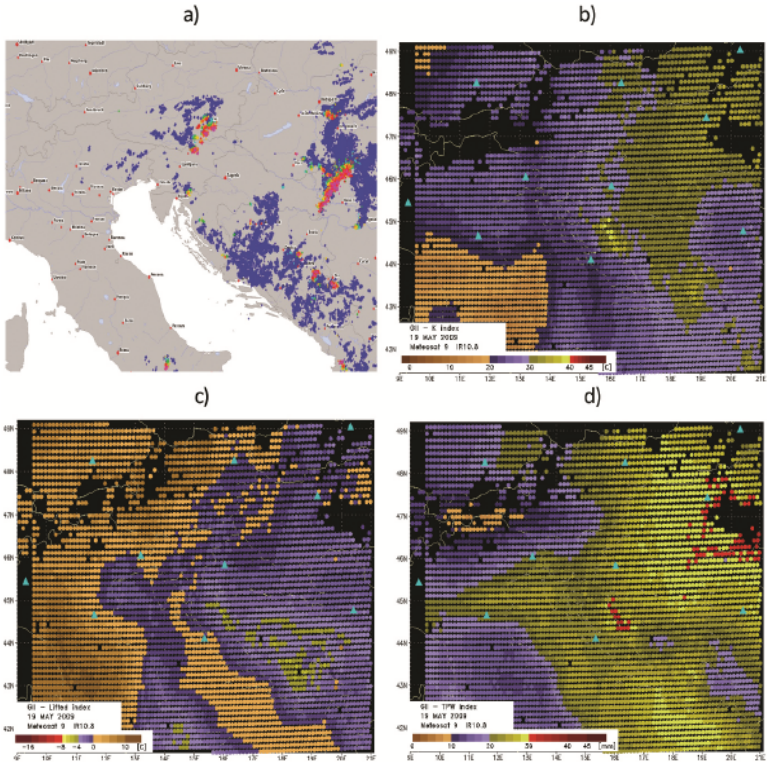

Figure 1. Distribution of lightning (a) in the period 08:00 to 18:00 UTC and spatial distribution of time-averaged value of K (b), LI (c) and TPW (d) index between 04:00 UTC and 08:00 UTC for the 19th May 2009. Blue triangles are marked positions of the observed radiosounding stations.

Last kind of verification is one done with radiosounding data, and it is also more objective approach. From this radiosounding data, values of four instability indices are gained and compared with 'satellite' indices at the point of sounding. That was done for 10 radiosounding stations in observed area, at 00:00 UTC.

4. Conclusions

Verification showed that the KO index was not efficient because of absence of 1000 hPa isobaric surface. A similar problem occurred with the generation of K index in areas where no isobaric surface was greater than 850 hPa. Full development of convection is followed 5 to 10 hours after the indices are showing instability, thus enabling the ‘forecast’ of convection. The differences between pointed areas of instability by indices and areas of actual convection development were sometimes present, mostly due to wind advection of air masses with prevailing winds. Favorable correlation between satellite-based and radiosounding-based indices, also normal distribution around zero of their difference, shows adequacy of PRM method. The results indicated the thresholds of instability indices somewhat vary from common values. Correction for the K index would be 10°C, for LI index -4°C and +20 mm for TPW indeks.

References

König, M., and E. de Coning, 2008: The MSG global instability indices product and its use as a nowcasting tool. *Weather Forecast.*, **24**, 72-85.

Rodgers, C. D., 1976: Retrieval of atmospheric temperature and composition from remote measurements of thermal radiation. *Rev. Geophys.*, **14**, 609-624.

Parameterization of the sensible and latent heat fluxes during bora wind in the Adriatic

Sanda Britvić Pejković*, Branko Grisogono**

**Meteorological and Hydrological Service of Croatia, Glagoljaska 11, Split, Croatia*
*** Department of Geophysics, Faculty of Science, University of Zagreb, Zagreb, Croatia*

1. Introduction

Evaluation of the vertical transport of heat, humidity and moment at the air-sea interface has been a subject of research of both meteorologists and oceanographers. There are no measurements of the heat fluxes over the Adriatic Sea, so a reliable parameterization is the only way to evaluate it. Different parameterization schemes, data sources and space-time averaging cause main problems for the accurate air-sea flux calculations. This paper focuses on the importance of different parameterizations for the different parts of the eastern Adriatic with special attention given to similarity theory and molecular effects that are included in COARE bulk algorithm. The difference between two parameterization methods has been analyzed at the Senj (northern Adriatic) and the Hvar (central Adriatic) stations.

2. Approach

Comparison between the two sensible and latent flux calculation methods has been analyzed. The first method of sensible and latent heat flux calculation is COARE 2.6 bulk algorithm. The second method is based on classic bulk equations with constant coefficients proposed by Gill (1982) and is often used in analysis of surface heat fluxes in the Adriatic Sea.

Fairall et. al. (2003) gave detailed explanations of COARE (Coupled Ocean-Atmosphere Response Experiment) bulk algorithm that is based on Liu et.al. (1979) model. Dorman et. al. (2003) used COARE bulk algorithm in the calculation of fluxes in the northern Adriatic and noticed that this code was developed and tested for noneqatorial regions as the Adriatic.

3. Description of experiment

The sensible and latent heat fluxes have been calculated from standard meteorological measurement and SST data at two meteorological stations: Hvar and Senj (data base of Meteorological and Hydrological Service of Republic of Croatia). From the analysis of available hourly averaged input parameters in the years 2002 and 2003 at the Hvar and the Senj stations, December 2002 has been chosen. In December 2002 input data set was complete for both stations and the results can represent importance of application of COARE bulk algorithm for the Adriatic area. That month was characterized by dominant bora wind, mainly light to moderate at Hvar and strong at Senj. That was the month with typical winter weather situation in the Adriatic area.

4. Results

The first analysis was the comparison between sensible and latent heat fluxes calculated by two parameterization methods for Hvar (Fig 1). The biggest differences between two heat flux parameterization methods were on 09-11 December and on 19-21 December, on the days characterized by light bora wind and strong sea minus air temperature difference after a frontal passage over the Adriatic. For that periods sea surface temperature was significantly higher than air temperature (up to 15.7 °C on December 20) and wind speed was low (lower than 4m/s).

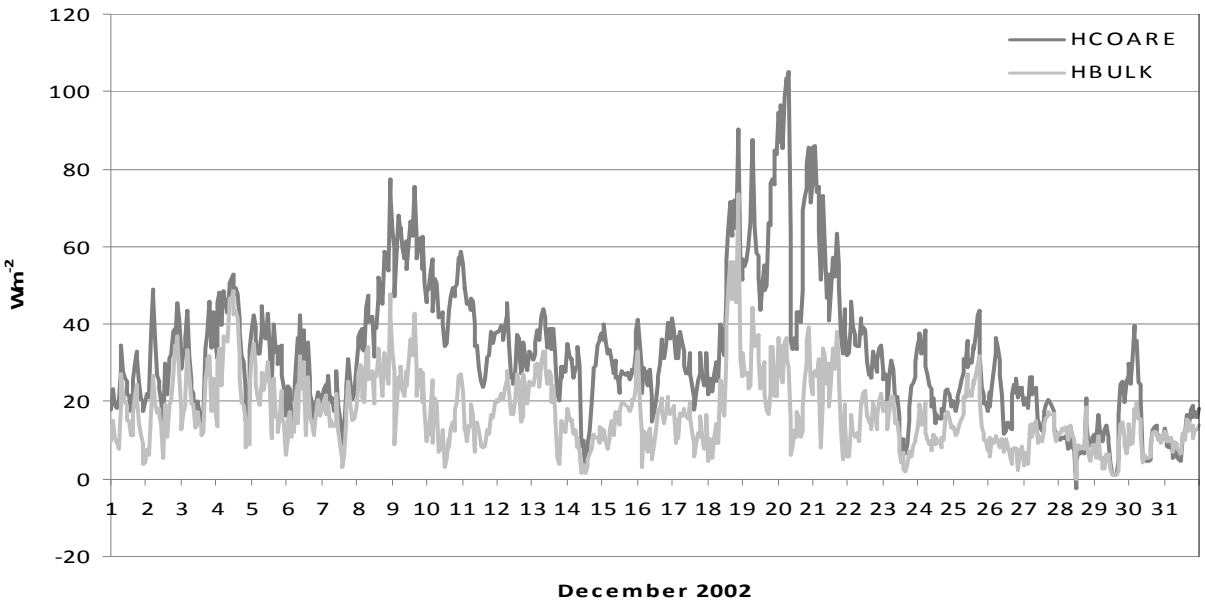

Figure 1. Hourly values of sensible heat fluxes calculated by COARE bulk algorithm (HCOARE) and bulk relations with constant coefficients (HBULK), Hvar, December, 2002.

The second analysis was the comparison between sensible and latent heat fluxes calculated by two parameterization methods for Senj. In December 2002 prevailing wind at Senj was also bora but generally much stronger than at Hvar. The sensible and latent heat fluxes calculated by two parameterization methods are generally similar at Senj (for latent heat fluxes are often smaller calculated by COARE bulk algorithm). During the light to moderate bora, sea minus air temperature difference is not so big because sea surface temperature is colder in the northern Adriatic than in the southern. This can also be a reason why calculations of fluxes by COARE bulk algorithm and bulk relations give similar results for Senj.

5. Conclusions

A detailed comparison between sensible and latent heat fluxes calculated by the COARE bulk algorithm and bulk equations with constant coefficients shows that maximal difference between the two methods is for light to moderate wind with unstable atmosphere when COARE bulk algorithm gives significantly larger amounts for both sensible and latent heat fluxes. This difference is more important for the central than northern Adriatic, mainly due to more frequent light to moderate bora together with big sea minus air temperature difference.

Inclusion of skin surface temperature instead of bulk temperature and inclusion of wave parameters into the surface roughness in the COARE bulk algorithm, can be the topic of future research.

References

Dorman, C.E., S. Carniel, L. Cavaleri, M. Sciavo, J. Doyle, T. Haack, J. Pullen, B.Grbec, I. Vilibić, I. Janeković, C. Lee, V. Malačić, M. Orlić, E. Paschini, A. Russo and R. P. Signell, 2007: February 2003 marine atmospheric conditions and the bora over the northern Adriatic. *J. Geophys. Res.*, **112**, 1-21.

Fairall, C.W., E. F. Bradley, J. E. Hare, A. A. Grachev, and J. B. Edson, 2003: Bulk parameterization of air-sea fluxes: update and verification for the COARE algorithm. *J. Clim.*, **16**, 571-590.

Gill, A. E. 1982: *Atmosphere-Ocean Dynamics*. Academic Press. Orlando, 662 pp.